Melt electrospinning for the production of osteochondral scaffolds with functional and compositional gradients

Gonçalo Nunes da Silva Carvalhão

Dissertation to obtain the Integrated Master degree in

Biological Engineering

Supervisors:

Joseph A. M. Steele, PhD

Professor Maria Margarida Fonseca Rodrigues Diogo

Examination Committee

Chairperson: Professor Arsénio do Carmo Sales Mendes Fialho

Supervisor: Professor Maria Margarida Fonseca Rodrigues Diogo

Member of the Committee: Professor Frederico Castelo Alves Ferreira

November 2016

Table of Contents

A. Abstract

The creation of functionalized materials offers the advantage of chemically tailoring surfaces that are useful for tissue engineering (TE). For that purpose, the processing technique to produce such structures must be precise enough in order to recreate the topographical geometry of living tissues.

Bearing in mind the need for this controlled surface engineering, it is hereby described the production of poly(ε-caprolactone) scaffolds through melt electrospinning materials functionalized with cell-binding peptides and antifouling polymer for the creation of gliding surfaces.

A hyaluronic acid–binding peptide (HA-BP) was synthesized using manual Fmoc solid-phase peptide synthesis, conjugated to PCL and processed by melt electrospinning to produce scaffolds. The same procedure was performed for another cell adhesion peptide, cRGDS. For polymer functionalization of materials, PCL was modified with an activators regenerated by electron transfer atom transfer radical polymerization (ARGET ATRP) initiator that was then melt electrospun and post-polymerized to create a poly(oligo(ethylene glycol) methacrylate) (pOEGMA) bottle-brush system through ARGET ATRP.

The presence of the functionalization elements on PCL surfaces was confirmed and the production of fibres was optimized to produce scaffolds aiming at the creation of platforms with different degrees of cell adherence.

Gliding and cell-adhesive surfaces such as those found in synovial joints, and cartilage and bone, respectively, are of great potential for the demanding therapeutic procedures and regeneration for osteochondral injuries.

Keywords: Melt electrospinning optimization, peptide-material functionalization, polymer-material functionalization, pOEGMA bottle-brushes, polymer brushes, surface-initiated ARGET ATRP.

A. Resumo

A criação de materiais funcionalizados permite a produção de superfícies quimicamente modificadas que são de extrema importância em Engenharia de Tecidos. Por este motivo, a técnica de fabricação destas estruturas deve ser suficientemente precisa para recrear a topografia de tecidos vivos.

Tendo em conta esta necessidade pela engenharia de superfícies para a medicina regenerativa, é aqui descrita a produção de *scaffolds* recorrendo à técnica de *melt electrospinning* para processamento de policaprolactona (PCL) funcionalizada com péptidos que promovem adesão celular e com um polímero que permite a criação de superfícies deslizantes capazes de impedir esta mesma característica.

Para tal, um péptido com afinidade para formar ligações com ácido hialurónico foi sintetizado recorrendo à síntese peptídica em fase sólida, conjugada ao material que serve de base aos *scaffolds*, PCL, e processada por *melt electrospinning.* O mesmo procedimento foi realizado para uma sequência peptídica usada para promover a adesão celular, cRGDS. No que diz respeito à funcionalização de PCL recorrendo a polímeros, este foi modificado com um iniciador de polimerização que foi posteriormente processado por *melt electrospinning* e o *scaffold* resultante foi polimerizado usando *activators regenerated by electron transfer atom transfer radical polymerization* (ARGET ATRP) para criar na sua superfície um sistema do tipo *bottle brush* composto pelo polímero poli(etileno glicol metacrilato) (POEGMA).

A presença dos elementos funcionalizantes na superfície de fibras de PCL foram confirmadas e a produção das fibras foi otimizada para produzir *scaffolds* com diferentes graus de adesão celular.

Superfícies deslizantes e superfícies que promovem a adesão celular tais como as das articulações sinoviais, e da cartilagem e osso, respetivamente, têm um grande potencial para o tratamento e regeneração de lesões osteocondreais.

Keywords: *Melt electrospinning*, funcionalização peptídica de materiais, funcionalização polimérica de materiais, *pOEGMA bottle-brushes*, *surface-initiated ARGET ATRP*.

B. Acknowledgments

First of all, I would like to thank professor Molly Stevens (Imperial College London, UK and Karolinska Institutet Stockholm, Sweden) for accepting me for this master thesis internship within her group at Karolinska Institutet. I will be forever grateful for this opportunity and for giving me the chance to work in the biomaterials field where I could learn a broad range of subjects from materials functionalization, processing and analysis to cell culture, tissue engineering and regenerative medicine. I would also like to thank for giving me the opportunity to attend TERMIS Uppsala 2016, where I could learn about ongoing and pioneering investigations in the field of tissue engineering and regenerative medicine.

I would also like to acknowledge my supervisor, Dr. Joseph Steele, who unconditionally supported me and my ideas through the length of the project and promoted my integration in the group.

I would like to thank to all the other people at KI from the division of biomaterials and regenerative medicine, namely Dr. Adam Gormley, for teaching me on peptide synthesis, Dr. Helene Autefage, who helped me planning cell assays with scaffolds, Dr. Paresh Parmar that kindly prepared the cRGDS-PCL conjugates, Dr. Christine-Maria Horejs and Dr. Christopher Grigsby for all the questions and thoughts on my project during the group meetings, and of course to my colleagues and friends Marco, Clotilde, Janina, Inês and Laura for making my staying in Stockholm even more enjoyable and for supporting me through these months.

To my professors at IST, for guiding me and for all the background that allowed me to perform this work, in special professor Margarida Diogo, professor Ana Azevedo and professor Angela Taipa.

To Joao for always being here for me and for all his support. Also, for always making me see the bright side out of hard times and obstacles.

This section could not be finished without my best friends Laura, Margarida, Mariana, Marta and Catarina, whose support and friendship started way before these final steps of my master degree. Finally, to my colleague and friend, Vitória, who always believed in me and my capabilities, and to whom I expect to be friends with for life.

C. List of Tables

D. List of Figures

E. List of Figures

(eq.)	Molar equivalents
(^{1}H-NMR)	proton nuclear magnetic resonance
3DP	3D printing
aa	Amino acid
AFM	Average fibre diameter
AM	Additive manufacturing
ARGET ATRP	Activators Regenerated by electron transfer ATRP
ARTP	Atom transfer radical polymerization
BiBB	α-bromoisobutyryl bromide
Boc	Tert-butyloxycarbonyl
CAD	Computer aided design
Cbz	Carboxybenzyl
DCM	Dichloromethane
DEE	Diethyl ether
DIPEA	N,N-Diisopropylethylamine
DMF	Dimethylformamide
ECM	Extracellular matrix
ESI-MS	Electrospray ionization mass spectroscopy
FDM	Fused deposition modelling
Fmoc	Fluorenylmethyloxycarbonyl chloride
HA	Hyaluronic acid or hyaluronan
HA-BP	Hyaluronic acid binding peptide
HBTU	2-(1H-benzotriazol-1-yl)-1,1,3,3-tetramethyluronium hexafluorophosphate
HFIP	1,1,1,3,3,3-hexafluoro-2-propanol
HPLC	High performance liquid chromatography
ME	Melt electrospinning
MEW	Melt electrospinning writing
Mn	Number average molecular weight
Mw	Weight average molecular weight
MW	Molecular weight
N^{α}	α-amino-protecting group
OEGMA	poly(ethylene glycol) methyl ether methacrylate
PCL	Poly(ε-caprolactone)
PEG	Poly(ethylene glycol)
PGA	Poly(glycolic acid)
PLA	Poly(lactic acid)
PMPI	p-maleimidophenyl isocyanate
pOEGMA	Poly[oligo(ethylene glycol) methyl ether methacrylate]
PS	Pore size
RP	Rapid prototyping
SE	Solution electrospinning
SEC	Size exclusion chromatography
SFF	Solid free form fabrication
SOP	Standard operating procedure
SPPS	Solid-phase peptide synthesis
TFA	Trifluoroacetic acid
TIS	Triisopropylsilane
TPMA	Tris[(2-pyridyl)methyl]amine

1. Introduction and state-of-the-art

1.1. Osteochondral tissues and their regeneration

Osteochondral tissues are those that form the synovial joints, namely cartilage and bone, including elbow, knee, ankle and shoulder joints. It is an interfacial tissue that is extended from the superficial cartilage to the underlying subchondral bone and, as such, is composed of hierarchical stratified zones that are represented in Figure 1.1.1, in which some chemical and histological properties are depicted.[1]

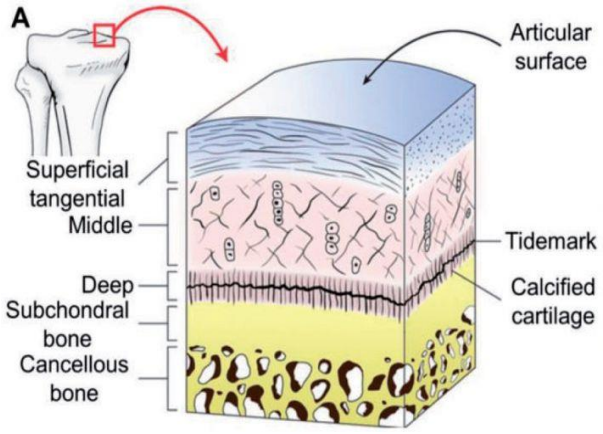

Figure 1.1.1 – Cross section of a typical osteochondral tissue. From Li et al. 2015[2].

Beyond the geometrical and histological complexities found in these interfacial tissues, the difficulty in producing constructs for osteochondral regeneration is exacerbated by the avascular, aneural and alymphatic character of cartilage which leads to its limited reparative properties when damaged. Bone, on the other hand, is a vascularized tissue with a nerve supply and constantly remodels through equilibrium between the deposition of new bone and resorption of the extracellular matrix (ECM) by osteoblasts and osteoclasts, respectively.[3] Despite this advantageous characteristic, large bone defects, as observed after bone tumour resections and severe non-union fractures, lack the template for an orchestrated regeneration and are not able to heal for themselves.[4]

The biomechanical purpose of synovial joints is to provide lubricated contact between the moving surfaces with as little frictional forces as possible, which is achieved by separating the cartilage layers by a thin film of fluid, the synovial fluid.[3] Considering the case of the knee joint, shown in Figure 1.1.2 in a simplified way, two osteochondral interfaces are represented and their mobility is preserved by their separation which is achieved by the synovial fluid produced by the synovial membrane – forming a gliding surface. These specialized surfaces are delicate and can be easily disrupted through trauma, infection or inflammation. In turn, this may lead to the formation of scar tissue – adhesions – that result from cellular ingrowth and bridging between previously gliding surfaces (red highlighted zone in Figure 1.1.2), leading to the restriction of movement and, hence, causing pain and compromised function.

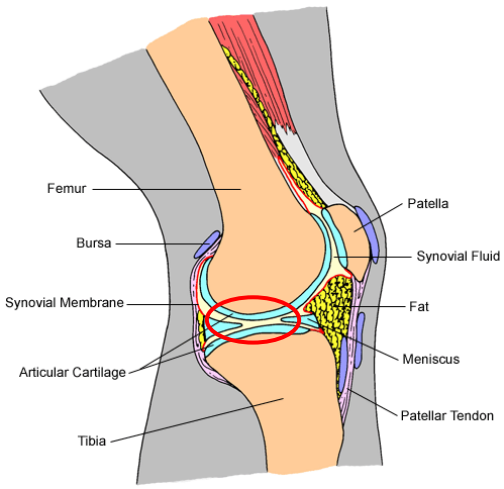

Figure 1.1.2 – Schematic organization of the knee joint.[5]

In light of the obstacles found in osteochondral tissues, the design of layered structures with both cell-adhesion (for tissue healing) and antifouling surfaces (to reduce cell ingrowth and allow the mobility between tissues) on opposing surfaces and in a controlled fashion is extremely interesting for tissue regeneration.

1.2. Biomaterials for osteochondral scaffolds

1.2.1. Biomaterial's requirements and general considerations for osteochondral scaffolds

Scaffolds play a crucial role in TE by providing a three-dimensional (3D) environment for cell seeding and proliferation, which is promoted by its physical structure and composition, often aimed at mimicking the *in vivo* environment.
General requirements in scaffolds for TE include biocompatibility, matching the mechanical properties of the target tissue, pore size and biodegradability of the construct. By being biocompatible, a scaffold possesses the ability to support normal cellular activity such as molecular signalling pathways without toxic long-term effects to the host tissues. Regarding the mechanical properties, the construct to be implanted must meet the mechanical properties of the target tissue to be regenerated as, for instance in bone and cartilage, the scaffolds must be able to support the weight of the body, being part of its supporting structure. This task is hampered by the need for highly porous structures to support cell attachment, proliferation and extra-cellular matrix (ECM) production.
The pore size in bone scaffolds should be at least 100 µm, and optimally in the range of 200 to 350 µm, with interconnected porosity in order to achieve successful diffusion of nutrients and oxygen, vascularization and continuous ingrowth of bone tissue.[6,7,8] Additionally, it has been shown that multi-scale porous scaffolds, involving both micro and macro porosities, show better results when compared to macroporosity alone.[9,10,11] However, porosity reduces compressive strength and increases the scaffold manufacturing complexity, although some techniques may be able to overtake this obstacle, such as melt electrospinning[12], further discussed in section 4.

According to the tissue engineering paradigm, the materials used in this type of constructs will be *resorbed and replaced over time by, and in tune with, the body's own newly regenerated biological tissue*[4], which explains the need for biodegradable materials. In the case of biodegradable polymers, used in this work, they generate more toxicity than non-degradable systems, as they degrade. However, biodegradable scaffolds are transient, supporting tissue formation, and subsequently resorbed in a controlled manner. Therefore no long-term structural or chemical complications compromise the formation of the new tissue.

It can be stated that an ideal scaffold for cartilage regeneration should be, apart from the other requirements referred above, osteoconductive (capable of promoting the differentiation of progenitor cells down an osteoblastic lineage), flexible, elastic, and nonantigenic, i.e. incapable of eliciting an immune response.[13]

For an ideal scaffold for bone, the construct must also be both osteoconductive and osseointegrative, meaning capable of supporting bone growth by promoting cell proliferation, adherence and formation of extracellular matrix (ECM) and encourage the ingrowth and integration into surrounding bone, respectively.[14]

In order to succeed in osteochondral scaffolds for biomedical applications, the complexity of the *in vivo* tissues should be considered relating to engineering, chemistry, biology and medicine.

1.2.2. Review of the existing biomaterials with focus on osteochondral regeneration

Biomaterials used for osteochondral tissue engineering consist, essentially, in bioactive inorganic materials, biological or synthetic polymers and composites of these.

Metals

Metals possess high compressive strengths and, therefore, are suitable for load-bearing clinical applications. However, unlike polymeric and other inorganic materials, metallic materials are not biodegradable. Furthermore, metallic materials develop interfacial fibrous tissue that isolates the implants from their surroundings and this fibrous tissue encapsulation is of concern due to excessive relative micromovement the device can cause at the bone–implant interface because of poor interfacial bonding. Nevertheless, there are some surface modification techniques that are often employed in order to improve bioactivity of these materials, such as in the case of titanium scaffolds.[15]

Furthermore, metal ions can be incorporated into polymers in order to promote osteogenesis. For instance, Woodfruff *et al.* 2013[16] produced melt-electrospun poly(ε-caprolactone) – strontium (PCL – strondium) substituted bioactive glass scaffolds were successfully proven to enhance higher alkaline phosphatase (ALP) activity of osteoblast precursor cells (MC3T3 cells) as well as increased osteogenic differentiation of the same cells.

Bioactive inorganic materials

The fragile nature of bioactive inorganic materials means that their fracture toughness cannot achieve that of bone and that they cannot be used alone in load-bearing applications[4].

As major constituent of bone, calcium phosphates, such as hydroxyapatite, beta-tricalcium phosphate and combinations of these known as biphasic calcium phosphate have been extensively studied in bone tissue engineering for scaffold fabrication[17].

Polymers

Polymers are of great interest in the area of TE, since they can be both bioactive and biodegradable and their properties such as mechanical strength and degradation rate can be tailored.[18]

Natural polymers, such as hyaluronic acid and collagen, are interesting options for osteochondral tissue engineering since they provide innate biological information to cells so as to guide them towards cell attachment and chemotactic responses. These polymers are, however, limited in sourcing, potentially prone to disease transmission and possess weak mechanical properties[4], which is the reason they are often reinforced by other materials in the form of composites[19]. Other examples of natural polymers are fibrin, alginate, silk and chitosan.

Regarding synthetic polymers, although they lack the innate biological information guidance to cells, they are often chosen over natural ones since they are flexible in being processed, easily tailored and capable of controlled degradation, with better lot-to-lot consistency[20]. Indeed, degradation of synthetic polymers such as poly(lactic acid) (PLA), poly(glycolic acid) (PGA), and PCL produces monomers which are quickly removed by the natural physiological pathway, allowing the osteoblasts to produce and substitute that volume with natural mineralization[17].

Composite materials

Biomaterial composites bring together advantageous properties of different materials, organic and inorganic, aiming at achieving a synergistic effect in their resultant properties. Succinctly, these composites encompass two phases, the dispersed and the matrix phase, in which the first one is usually harder and stiffer, aiming at the immobilization of the matrix phase, while the matrix phase acts primarily as a stress transfer medium.[21]

1.3. Scaffold fabrication techniques

1.3.1. Review of the existing fabrication techniques

There are several methods extensively studied for the manufacturing of porous scaffolds, such as chemical/gas foaming[22], solvent casting and particulate leaching[23,24], freeze-drying[25,26], thermally induced phase separation[27,28,29], fibre meshing[30] and sol-gel[31]. However, these techniques do not directly control pore size, shape and interconnectivity.[32] Moreover, solvent casting and particulate leaching are also liable to retain toxic solvents within the polymer used and to denature proteins and other molecules incorporated into the polymer by the use of solvents[33]; fibre meshing leads to a low structure stability of the scaffolds, although they possess a large surface area for cell attachment and a rapid diffusion of nutrients in favour of cell survival and growth[34,35]; and freeze drying produces small pores ranging from 20 to 100 µm, which in some cases can be insufficient for cell migration and new bone tissue ingrowth.[36]

Aiming at overtaking these limitations, additive manufacturing (AM) approaches such as 3D printing (3DP), solid freeform fabrication (SFF), rapid prototyping (RP) and melt-electrospinning writing (MEW) arose. AM is a broad term for an increasing number of techniques in which complex structures are constructed in a layer-by-layer fashion according to computer aided design (CAD).[37] Each layer can be built to have a specific morphological configuration to achieve the desired micro- and macrostructure of the scaffold. TE benefits from AM due to the possibility of manufacturing custom-shaped implants with controlled internal and external architecture based on medical imaging data.[19]

Although 3DP, RP and SFF techniques show large advantages over traditional methods for the production of porous scaffolds, these still present some limitations. 3DP is limited by the use of organic solvents as binders due to dissolving of commercial print heads and difficulty in removing unbound powder from small or curved channels.[38] Also, with SFF techniques, such as fused deposition modelling (FDM), a technique based in melt-extruded scaffolds with resulting fibre in the range of 100 to 500 µm, smaller filaments diameters are difficult to achieve. Reaching these smaller molten filaments would improve the flexibility and conformity of pore organization within the scaffold.[39] Using FDM for direct writing would wind up challenging as polymer degradation occurs when making a thermoplastic polymer pass through a small diameter nozzle.[40]

Smaller diameter fibres can be achieved by using solution electrospinning (SE), an established process for the production of continuous fibres from a fluid where electrical instabilities are utilised to produce submicron fibres. This, however, leads to a lack of control in fibre deposition and it has limited reproducible geometry. This uncontrolled fibre deposition fashion then leads to small pore sizes, which act as a barrier to cell infiltration rather than promoting it[40,41]. In this work, melt electrospinning, which shows a higher control over the deposition of fibres, is used. This scaffold fabrication technique is further described in sections 4.1.1 and 4.1.2.

1.4. Scaffold's surface functionalization

As cells are inherently sensitive to their surroundings, appropriate osteoinductive cues can be incorporated into scaffolds in order to promote the attraction and adhesion of the patient's own stem cells after scaffold implantation. Indeed, adhesion of cells is a prerequisite for their subsequent proliferation and differentiation.[42] Moreover, the modulation of characteristics such as roughness, porosity, chemical and biological composition allows the regulation of material integration within the body as well as the guidance of specific responses, such as cell adhesion, detachment, proliferation, differentiation, or metabolic activity.[43]

In addition to being able to substitute for ECM proteins, short peptide sequences supply a less system variability than naturally derived proteins and, when considering synthetic sequences, they are simple to graft to a surface by introducing a range of functional groups.[44] Therefore, short peptides are candidates for surface functionalization aimed at cell adhesion.

The canonical peptide sequence used for cell adhesion is the arginine-glycine-aspartic acid, RGD. This general cell-adhesion sequence is widely found in ECM proteins and recognized by integrins, transmembrane receptors that are bridges for cell-cell and cell-ECM interactions. *In vivo* studies performed in animal models have reported that implant materials coated with RGD containing peptides improve early bone formation around implants.[45,46]

Another peptide, concerning cartilage engineering, is a hyaluronic acid binding peptide (HA-BP) that specifically and non-covalently binds HA and is used in order to mimic the dynamic nature of native ECM and protein–GAG interactions. This peptide, of amino acid sequence RYPISRPRKR, was derived from the HA-binding region of the link protein which stabilizes the interaction between HA and the proteoglycan aggrecan in articular cartilage.

In spite of the importance of surfaces to be able to promote cell attachment, the creation of gliding surfaces, i.e., antifouling for cell adhesion, can also be very useful in several medical applications as stated and described in section 1.1.Harrison *et al.* 2015[47] have successfully shown the production of a zonally-functionalised scaffold. They electrospun fibres composed of PCL end-functionalized with a polymerization initiating group (BiBB) that resulted in PCL scaffolds with an antifouling surface capable of avoiding cell adherence. This functionalization is hereby recreated and applied to melt electrospinning.

1.5. Description of the concept of the work proposed

The main goal of this work was to produce geometrically-controlled and functionalized fibre meshes in order to promote several levels of cellular adhesion needed as tools for TE, with focus on osteochondral lesions.

In order to do that, peptides and polymer bottle-brushes were fabricated in order to functionalize the surface of melt electrospun PCL scaffolds.

The first part of the project consisted in producing the peptide sequences to promote cell adhesion and to bind hyaluronic acid.

For the peptide functionalization of the PCL polymer, the hyaluronic acid binding-peptide (HA-BP) and a cyclised version of RGD, cRGDS, both used previously by the group with solution electrospinning (Chow *et al.* 2014[48] for the HA-BP and Harrison *et al*. 2015[47] for cRGDS) were selected. This version of the RGD peptide, cRGDS, was used as it has long been recognized that the RGD sequence loses affinity and specificity when presented outside the context of the native protein.[49,50] The activity of the sequence can be improved by adding surrounding amino acids (aa) from the native sequence[51], and by cyclizing the peptide, as this is most likely to exist in an exposed loop conformation in ECM proteins such as fibronectin.[52,53]

After synthesized recurring to Fmoc solid phase peptide synthesis, these peptides were conjugated to low molecular PCL. In order to produce the peptide-polymer conjugates, the peptides comprised the bioactive sequence (cRGD and HA-BP) and a CGGG (a cysteine, and three glycines) sequence to link the bioactive sequence to the biomaterial. The glycines served as spacers and the cysteine on the N-terminus was coupled to the PCL by reacting the thiol side chain of the cysteine with the maleimide group of the linker molecule, p-maleimidophenyl isocyanate, in a Michael-type addition.[54] The representation of the final peptide-polymer conjugates in the case of HA-BP is shown in Figure 1.5.1. It is worth noting that the reaction occurs in both ends of PCL chains and that low MW PCL (M_W 14 000) was selected to prevent water solubility of the conjugates and effectively anchor them to the bulk fibres.[48]

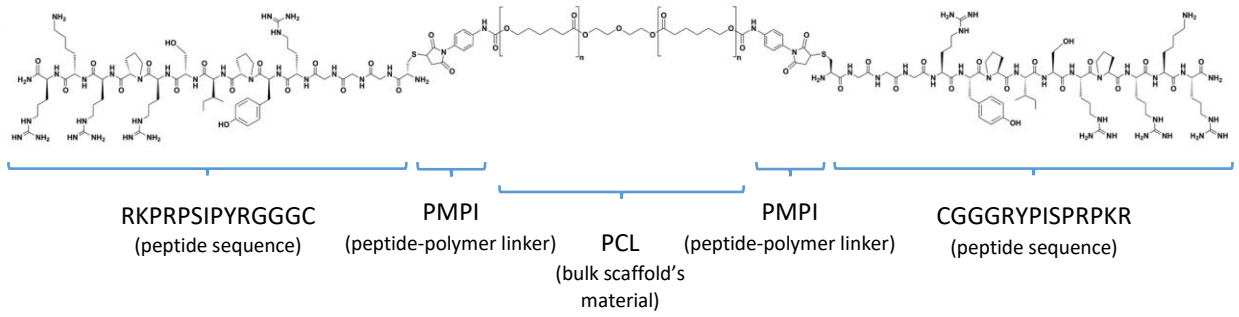

Figure 1.5.1 – Chemical structure of the hyaluronic acid – binding peptide (HA-BP) – PCL conjugate with the specific binding sequence RYPISPRPKR. Adapted from Chow et al. 2014[48].

For the polymer functionalization, p(OEGMA) bottle-brushes were produced by using ARGET ATRP polymerization reaction in pre end-functionalized PCL surfaces with the polymerization initiator, α-bromoisobutyryl bromide (BiBB). The chemical organization of the end-functionalized PCL with the p(OEGMA) brushes is represented in Figure 1.5.2 and the description of this stage of the project is further described in section 3.1.

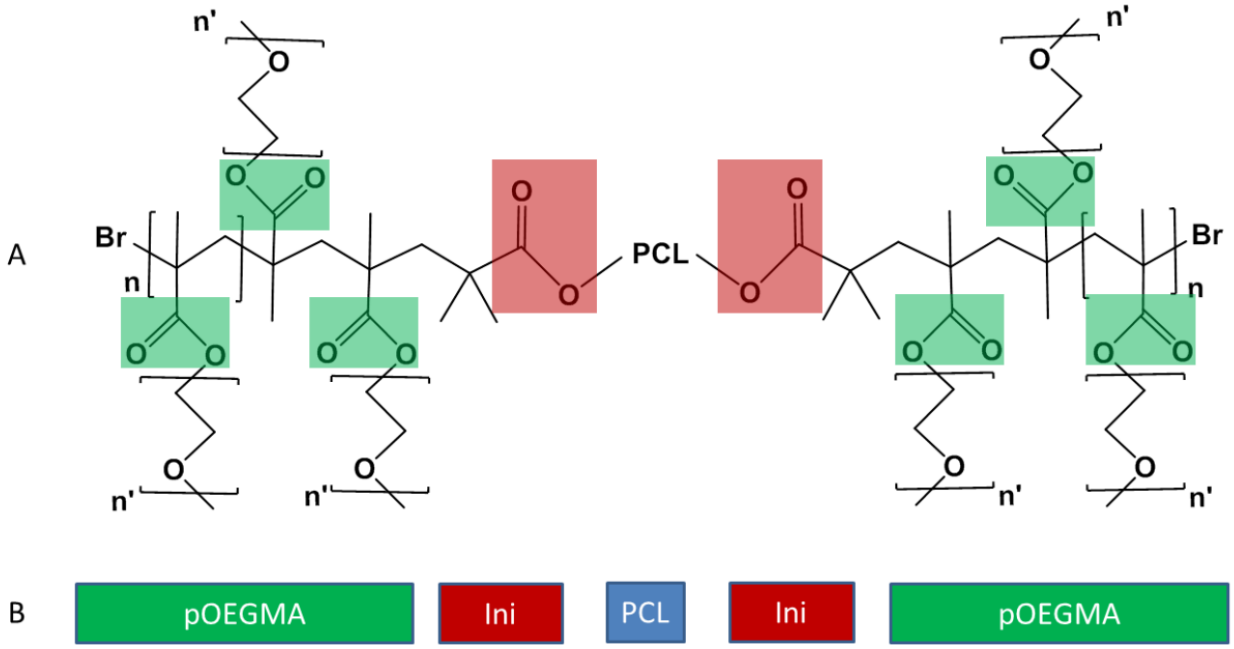

Figure 1.5.2 - Chemical structure and schematic of modified PCL-ini with pOEGMA polymer brush grafted from both ends of the polymeric chain. Red shaded regions indicate the ester linkages binding a whole polymer bottlebrush to the PCL, originating from the initiator group, and green shaded regions indicating the ester bond binding a "branch" or single OEGMA unit to the bottlebrush backbone. (B) Schematic representation of the polymer structure with the PCL (blue) portion, the structural contribution of the BiBB initiator (red), and the pOEGMA bottlebrush (green).[55]

The second part of the project consisted in the optimization of PCL printing using melt electrospinning, namely in a 50% (w/w) 45-80 kDa PCL blend that was found to print in a stabilized way. Melt electrospinning is a relatively new technique for the controlled deposition of polymer fibres and the functionalisation of these fibres was pioneered in this work.

As the physicochemical properties of the peptide conjugates and the polymerization initiator are different from the ones of the PCL, namely referring to their charge, each one of the resulting blends has different physicochemical properties and an optimization for each functionalized PCL was required.

The stages of the proposed project are schematically represented and summarised in Figure 1.5.3.

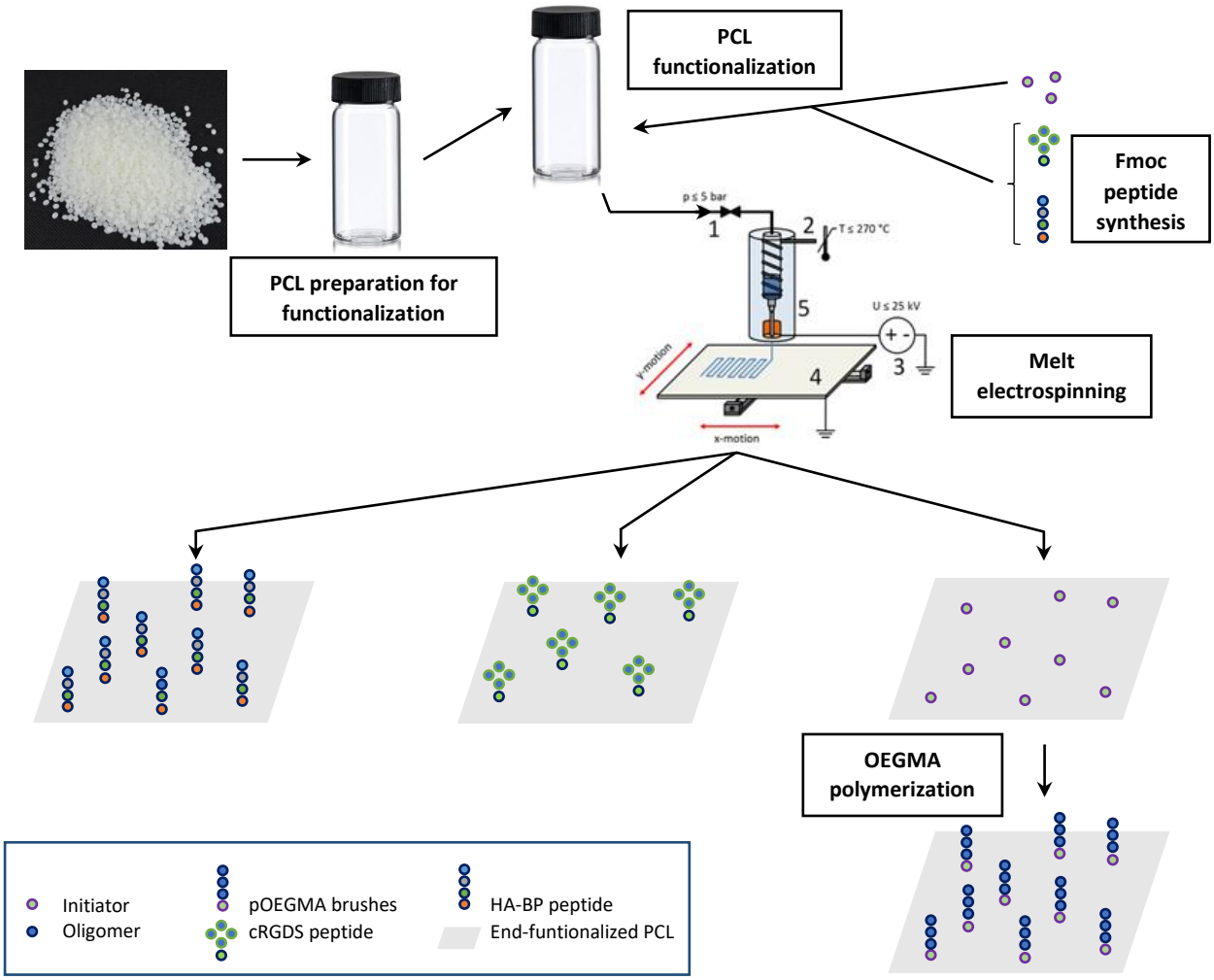

Figure 1.5.3 – Schematic representation of the main stages of the project.

Although melt electrospinning processing and the production of the decorating motifs were performed simultaneously, the first is presented in the last chapter of this thesis, and the seconds are explained in chapter 2 and 3. To prove the surface functionalization of the bulk material for scaffolds, in these two chapters, work from chapter 4 is presented, but only explained in this last chapter.

2. PCL peptide functionalization to promote scaffold cell adherence

2.1. Introduction

Peptide synthesis based on chemical methods has over 100 years of history, since the production of the first N-protected dipeptide, and has grown exponentially since the invention of solid phase peptide synthesis (SPPS) by Merrifield, in 1963, when a tetrapeptide was achieved by using the carbobenzoxy (Cbz) as an α-amino-protecting group (N^{α}). In 1967, he then modified the method to use a new protecting group, t-butyloxycarbonyl (Boc), which was firstly used for manual peptide synthesis and that served as base for the construction of the first automated solid phase synthesizer, also by Merrifield, in 1968.[56]

Protecting groups allow for the controlled and sequential addition of amino acids (aa) to a specific peptide sequence, that otherwise would polymerize during coupling.

In 1970, the 9-fluorenylmethoxycarbonyl (Fmoc) group for N^{α} protection was presented by Carpino and Han[57]. The cleavage of the Fmoc group is performed using a moderate base and this group is also stable in acidic conditions, offering a chemically mild alternative to the acid-labile Boc group. Also, the elimination of repetitive moderate acidic steps and the final strong acidic step present in Boc was envisioned as being more compatible with the synthesis of peptides that are susceptible to acid-catalysed side reactions. Additionally, Fmoc chemistry does not require special equipment and is relatively safe when compared to Boc, which was why Fmoc chemistry was adopted for solid-phase applications in the late 1970s.[58]

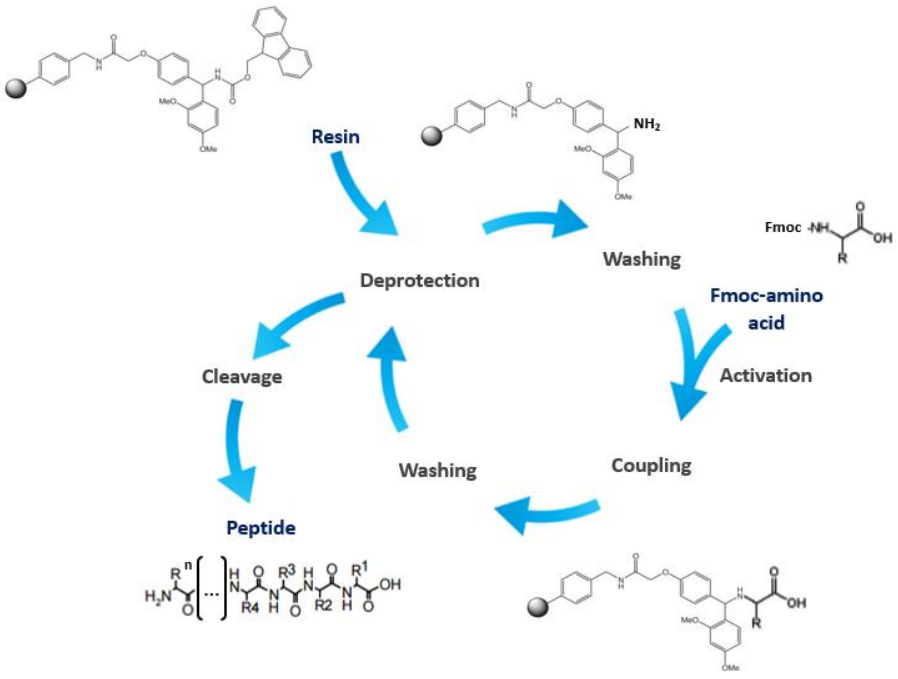

Figure 2.1.1 – Cyclic process of Fmoc peptide synthesis recurring to a Rink resine. Adapted from Duro-Castano et al. 2014[59]*.*

The process used for manually synthesizing peptides on a resin, the solid support for peptide building through the sequential addition of amino acids, is shown in Figure 2.1.1.

As described in section 2.2.1, firstly the Fmoc-protected resin is swollen and the N^{α} protecting group is removed before the addition of the first Fmoc-protected amino acid, activated by HBTU. Once the amino acid is coupled to the resin, it is filtered and washed to remove byproducts and excess reagents. Following this step, the Fmoc group is removed and the resin is washed, leaving the resin-peptide ready for the next coupling cycle. The cycle is repeated until the peptide sequence is complete and, after removal of the final protecting group, the peptide is cleaved from the resin.

This cyclic method was used to synthesize the peptides, cRGDS and HA-BP, for posterior peptide functionalisation of PCL and for the production of a biotinylated monomer (section 3.2.2) for versatile polymerization of p(OEGMA-co-biotin) on surface initiated PCL.

To conclude the assessment of the peptides on the surface of PCL fibres processed by ME (described in section 4.2.2), these fibres were fluorescently labelled with HA – fluorescein and the fibres were analysed using the fluorescence microscope. The schematic representation of this step is shown in Figure 3.1.6.

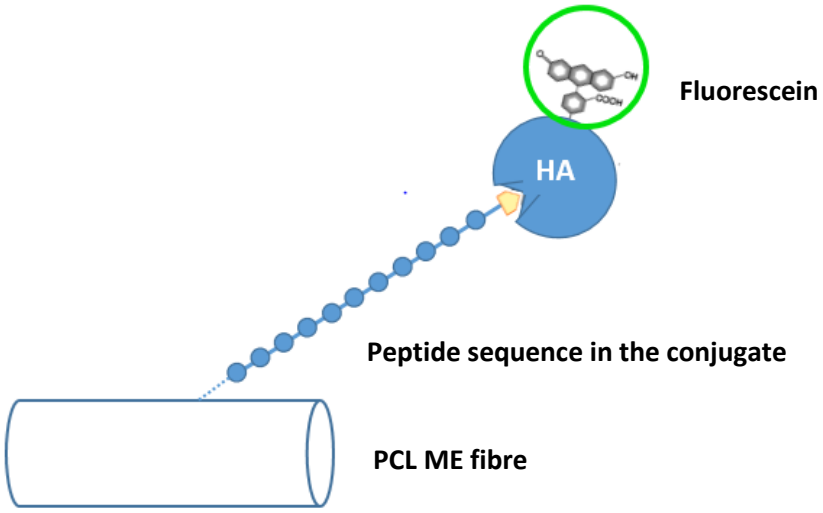

Figure 2.1.2 – Schematic representation of the HA-fluorescein labelling of peptide-polymer conjugates on the surface of scaffolds.

2.2. Materials and methods

2.2.1.HA-BP synthesis and purification

The 14-aa peptide sequence (CGGGRYPISRPRKR) was synthesized by manual Fmoc solid-phase peptide synthesis (SPPS), using a 50 mL peptide synthesis vessel (Synthware Glass) and a nitrogen-bubbling system (Schlenk line). Fmoc-Rink-Amide aminomethyl polystyrene resin (100-200 mesh, 0.56 mmol/g functionalization) the solid support for the

synthesis, Fmoc-protected aa and Benzotriazole-N,N,N',N'-tetramethyluronium-hexafluoro-phosphate (HBTU), the coupling agent, were purchased from AGTC Bioproducts (UK), as well as diisopropylethylamine (DIPEA) and dithiothreitol (DTT). Solvents, dimethyl formamide (DMF) and dichlomethane (DCM) were purchased from Honeywell (Sweden). Trifluoracetic acid (TFA), triisopropyl silane (TIS) and Piperidine purchased from Sigma Aldrich (Sweden). All reagents were synthesis-grade.

The protocol used was adapted from Chow *et al.*[48] 2014 for a 0.25 mM scale. Firstly, and before aa adition, the resin was swollen for 30 min in DCM and deprotected by a solution of 20% (v/v) piperidine in DMF and then washed with DCM and DMF. Each aa was, then, coupled to the growing peptide sequence by adding an activated solution of HBTU and DIPEA (3.95 and 6 eq., respectively, to 4 eq. of aa) for 1.5h. After each deprotection and coupling, and to confirm if each of these steps worked, Nihydrin tests (NT, Kaiser tests, Sigma Aldrich) were performed at 100 °C to assess the presence of free amines. After finishing the peptide sequence, and following the Fmoc-deprotection of the last aa, the peptide was cleaved from the resin for 4h in a cleavage solution composed of 2.5% (w/v) of DTT in 95% TFA, 2.5% TIS, and 2.5% DI water. After recovery of the cleaving solution plus the peptide, TFA was removed by rotary evaporation.

In order to recover and perform an intermediate purification, the peptide residue solution was precipitated with cold diethyl ether (DEE) and washed with DEE and Millipore water to allow the removal of residual amino acids and other reagents. After new washings with DEE, the precipitate was dried under nitrogen and this process was completed by overnight drying in a vacuum desiccator.

In the purification step, the peptide was dissolved in a solution of 5% acetonitrile (ACN, AGTC Bioproducts), 0.1% TFA and ultrapure water, which was passed through a 0.45 µm filter and injected into a reverse phase preparative high performance liquid chromatography (HPLC). The HPLC was performed by running a mobile phase gradient of 95% ultrapure water and 5% ACN to 100% ACN with 0.1% TFA.

Finally, the solution containing the purified peptide was rotary evaporated to remove residual ACN and TFA, frozen to -80°C and freeze dried.

2.2.2.HA-BP – PCL conjugation

To prepare the peptide-polymer conjugates, the terminal hydroxyl groups of PCL (M_w 14 kDa) were modified with p-maleimidophenyl isocyanate (PMPI) to generate a maleimide-functionalized PCL. The peptides were then coupled to the PCL-maleimide by reacting the thiol side chain of the cysteine with the maleimide group via Michael type addition.

2.2.2.1. PCL-PMPI conjugation

In this scheme for the conjugation, an adapted protocol from Chow et al. was used. In brief, PCL (Sigma, M_W 14 kDa) was dissolved in anhydrous DMF at 250 mg/mL in a round bottom flask previously covered and sealed with a rubber septum and maintained under positive pressure with dry nitrogen. The addition is performed under anhydrous conditions as the reaction of the PCL with PMPI can't be performed in the presence of water. The dissolution of the PCL in the solvent was promoted by adding a small stir bar and by sonicating the solution.

After complete dissolution, p-maleimidophenyl isocyanate (Chem-Impex International, Inc.) at 15-fold molar excess to PCL was dissolved in anhydrous DMF and added drop-wise to the PCL solution. The resulting solution was bubbled with nitrogen for 15 minutes and was allowed to react under low stirring rate over night. At the end of the reaction, the conjugation reaction was confirmed by ^{1}H NMR and the product was precipitated and washed with cold DEE and then with water to remove the unreacted PMPI. Finally, the purified product in water was frozen to -80°C, freeze-dried and stored at 4°C.

2.2.2.2. PCL-PMPI – peptides conjugation

cRGDS peptide conjugates were kindly prepared and purified by Dr. Paresh Parmar (Stevens Group, Imperial College London, UK).

For HA-BP, the purified peptides and PCL-PMPI were dissolved in anhydrous DMF separately with a 4 molar excess of peptide. Each peptide was then added to the PCL-PMPI solution and stirred overnight. The resulting conjugates were precipitated and washed with cold DEE and washed with water to remove the excess of peptide and then dried under vacuum before storage at 4°C.

2.2.3. Assessment of HA-BP and cRGDS in the melt electrospun fibres' surface

The functionality of biotinylated HA-BP in the final melt electrospun fibres was assessed visually by binding HA-fluorescein isothiocyanate (FITC). Samples were first blocked in 0.1% (w/v) bovine serum albumin (Sigma Aldrich) in PBS, followed by 0.5 mg/ml FITC-HA (Millipore, Sweden) in PBS for 1h at 37°C. Samples were washed in PBS to remove unbound FITC-HA and imaged on a Zeiss Axio Imager M2 upright epifluorescent microscope, relative to unfunctionalised and cRGDS-functionalized controls.

2.3. Results and discussion

2.3.1. Synthesis of HA-BP

After synthesizing the HA-BP, the MW of the final product before purification was confirmed by electrospray ionization – mass spectroscopy (ESI-MS). The expected molecular weight was 1602.87 g/mol calculated by inserting the 14-aa sequence in an on-line software, Pepcalc.com (Appendix 6.2). The ESI mass spectrum obtained is shown in Appendix 6.1 , where a fragment of 802 g/mol is evidenced. This value multiplied by a factor of two results in a 1604 g/mol MW, less than 2 g/mol of difference from the expected value. This deviation was explained by some chemical impurity that bound to the peptide chain. In spite of this difference, it was considered that the correct and full peptide sequence was produced. As a matter of fact, the most important factor relied on the functional binding of HA.

2.3.2. Assessment of the peptide-functionalized PCL scaffolds

In order to prove PCL surface-functionalization with the peptides, the lasts and a PCL control were stained with HA – fluorescein. After the washing step, which washes out the HA that wasn't bind to the peptides on the surface, scaffolds were imaged using fluorescent microscopy. Since HA – BP specifically binds to HA (it's derived from the HA-binding region of the link protein) and RGDS is a general cell-adhesion sequence, it is expected that the fluorescence intensity increases in the order, PCL control, PCL – cRGDS and PCL – HA – BP.

In Figure 2.3.1 (A), one can observe that this PCL scaffold is showing minor auto fluorescence and negligible non-specific binding of HA-FITC, as there are not specific fluorescence sites. Regarding Figure 2.3.1 (B), the localized fluorescence on the fibres is more pronounced, indicating some non-specific binding to the charged cRGDS peptide. The HA – BP scaffold in Figure 2.3.1 (C) shows a significantly greater fluorescence intensity, indicating that the surface was successfully enriched in functional HA-binding peptide. The difference in intensity between the cRGDS and HA-BP scaffolds indicates that the HA-FITC binds with greater affinity to the HA – BP sequence.

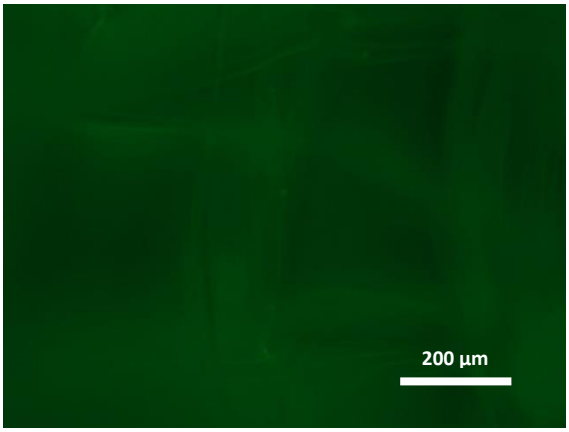

(A)

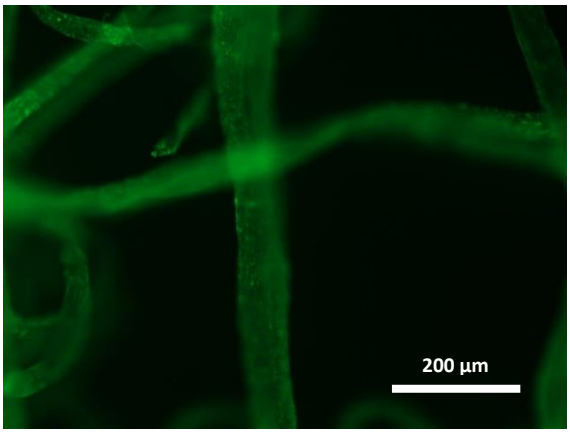

(B)

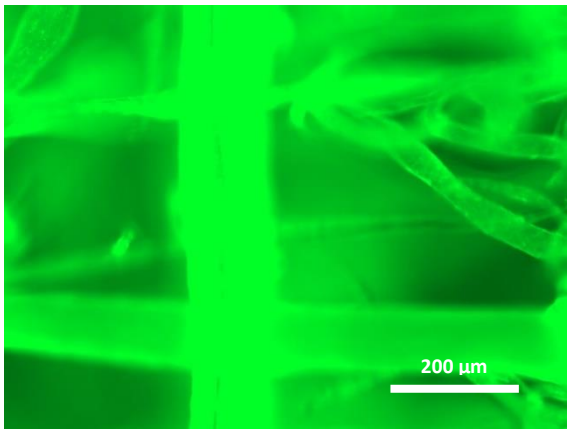

(C)

Figure 2.3.1 – Fluorescence micrographs of PCL control (A), PCL-cRGDS (5% (w/w)) (B) and PCL-HA-BP (5% (w/w)) (C) with HA – fluorescein labelling (10x).

2.4. Conclusions

Peptide synthesis and conjugation to PCL was successful, as validated by ESI-MS and ^{1}H-NMR. Furthermore, it was proven that fibres possessed peptides on their surface following ME printing. This was confirmed by HA-fluorescein labelling and imaging of scaffolds. This work was the first instance of peptide-polymer conjugates being applied to melt-electrospinning.

3. Controlled radical polymerization for the creation of gliding PCL surfaces

3.1. Introduction

As polymers are highly tailorable concerning their design, properties and architecture, they are excellent candidates not only for the production of materials, but also for the modification of its surfaces. This makes them of great interest for TE, where materials must meet several requirements for integration *in vivo* and promotion of regeneration where needed.

Free radical polymerization (FRP) is one of the several approaches that can be used to produce polymers. It is an extremely versatile method, as a large range of monomers (most vinyl monomers) may be polymerized or copolymerized and the reaction conditions are mild, since the temperatures range from 0 to 100 °C and water and other impurities are well tolerated. As so, FRP has become the most widespread industrial method for the production of polymers such as plastics and rubbers. However, the reaction requires the absence of oxygen.[60]

FRP is a polymerization method by which a polymer is formed by the production of free radicals and the successive addition of free radical building blocks. It is divided in three different kinetic stages: initiation, propagation and termination, shown and chemically described in Figure 3.1.1.

Initiation occurs when the radical is produced in the presence of a vinyl monomer unit (functional group –CH=CH_2), followed by the addition of this radical to the double bond of the monomer and resulting in the formation of the radical monomer unit. Propagation consists in the lengthening of the chain, which is promoted by the attack of this resulting radical monomer unit to the vinyl unit of another monomer, resulting in the formation of a new radical comprised by two monomer units. This process, which is characterized by growing of molecular weight, propagates until radicals react together to form a stable paired electron covalent bond, known as termination, where the radical reactivity is lost.

Figure 3.1.1 – Schematic representation of the steps of initiation, propagation and termination found in FRP, adapted from.[61]

This FRP polymerization reaction results in polymers with poorly controlled architecture and molecular weight distribution, which then reflects in their mechanical and physical properties. In TE-related applications, the control of these properties are of extreme relevance, as the aim consists in creating platforms with very specific requirements. Therefore, in the 1990s, several methods of controlled radical polymerization (CRP) were developed, in which the synthesis of a polymer with a predictable molecular weight and a narrow molecular weight distribution,

polydispersity index (PD, M_w/M_n, Đ < 1.5) between polymer chains is accomplished in the same reactor. Other advantage granted by CRP techniques is the linear evolution of number average molar mass, M_w, with time, which easily allows the production of the M_n desired. Moreover, this reaction control allows polymerization reaction to be performed in stages, which further allows the end group to be maintained and be used to either re-initiate the polymerization and further grow the polymer chain, or functionalization with other compounds.

Examples of CRP include reverse addition fragmentation polymerization (RAFT), atom transfer radical polymerization (ATRP) and activators regenerated by electron transfer atom transfer radical polymerization (ARGET ATRP).

ATRP, developed in 1995, has been successfully used to produce polymer brushes for biological systems in order to produce haemocompatible and thermoresponsive surfaces to control cell adhesion. However, this technique has several drawbacks when considering cytotoxicity, as high concentrations of potentially toxic transition metal catalyst are used together with organic solvents. This major drawback can be overtaken by using a modified form of conventional ATRP that was presented in 2005, ARGET ATRP.[55]

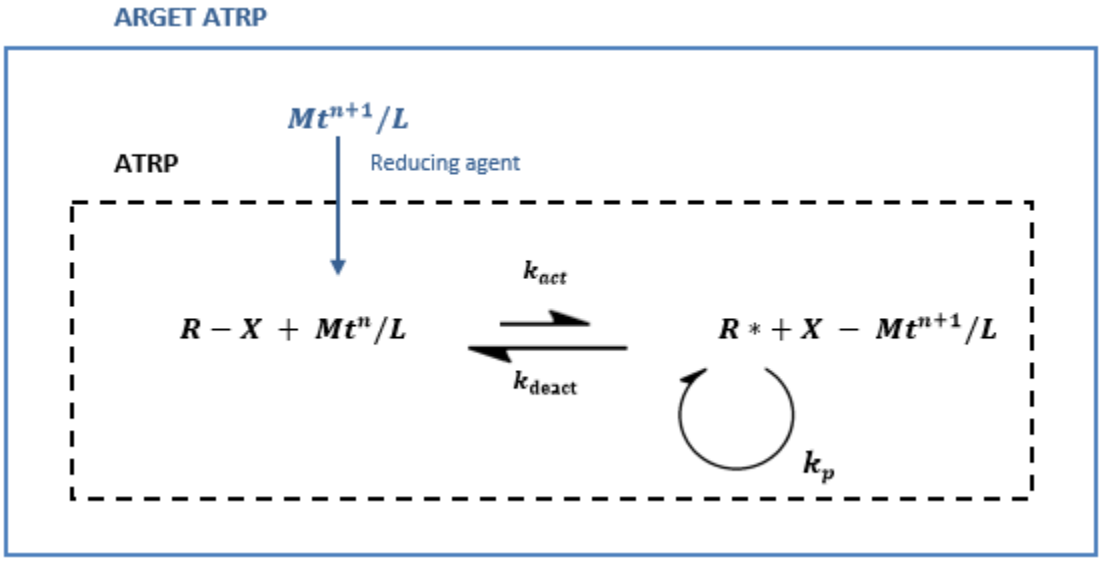

R	Part of a haloalkane initiator and polymer chain	k_{act}	Activation rate constant
X	Cl or Br	k_{deact}	Deactivation rate constant
Mt^n	Metal catalyst	k_p	Propagation rate constant
L	Ligand		

Figure 3.1.2 – Schematic of ATRP and ARGET ATRP polymerization reactions. Adapted from [61].

ARGET ATRP differs from conventional ATRP (Figure 3.1.2) by the use of a reducing agent, ascorbic acid for instance, which allows the use of a significantly reduced concentration of the potentially toxic catalyst to be used. This is due to the continuous recycling and production of the catalyst in the reduced state[62], i.e., reduction of the Cu(II)/ligand to Cu(I)/ligand form. The reaction then follows as the conventional ATRP method, which relies on the reversible redox reaction of a dormant haloalkane terminated polymer chain, R, and through the transfer of a halogen, X, to a transition metal complex, Mt^n/L, generating a free and active carbon centered radical at the chain end, R^*, and

resulting on the oxidation of the transition metal complex, $X - Mt^{n+1}/L$. The oxidized form of the transition metal catalyst then reacts and reconverts the propagating radical chain end, R^*, to the corresponding halogen-capped dormant species.[63]

ARGET ATRP has been successfully used for surface-initiated polymerizations, also known as *grafting from*, as this polymerization technique is extremely versatile and offers excellent control over chain length, architecture, reaction kinetics and a large number of monomers can be incorporated, resulting in a panoply of surface properties.[64,65] *Grafting from* is achieved by the covalent attachment of an initiating group to the surface, which generates a radical that reacts with a monomer unit in solution and allows the polymer to grow from the surface. Moreover, and important for this work, this method avoids the steric hindrance, which can lead to high-density surface functionalization.[66,67]

However, grafting polymers from surfaces within a solution promotes the creation of chemical gradients within the reaction vessel, namely the low local concentration of the deactivating Cu(II) adjacent to the reacting surface, which can lead to a local loss of control of the reaction. The use of a *sacrificial initiator*, ethyl-α-bromoisobutyrate (EBiB), in solution can solve this drawback, as this will also lead to the polymerization throughout the solution and avoiding the creation of the chemical gradient. Moreover, as the polymerization occurs both in solution and from the surface in the same reaction vessel, i.e., under the same conditions, the results from the analysis of the solution can be translated to the ones on the surface-grafted polymer.[68] The use of the *free polymer* as *surrogate* for the surface bound polymer has been shown in the literature to be a reliable method to monitor and control the M_n and M_W/M_n for the polymers grown from surfaces within reaction vessels.

After the reaction, and for further characterization of the resultant surfaces, these will have to be washed so as to remove any free polymer formed in solution.

In this work, the covalent attachment of the initiating group (BIBB) was achieved by end-functionalization of both ends of PCL chains with BIBB, with the chemical structure demonstrated in Figure 3.1.3.

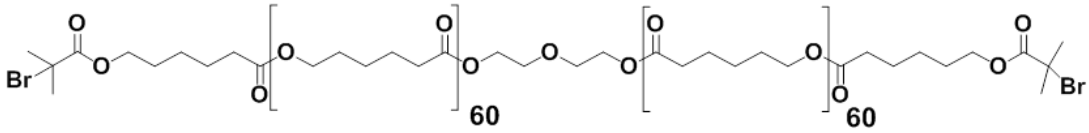

Figure 3.1.3 - End functionalised PCL-diol with the initiating group BIBB (PCL-Ini). From[55].

The monomers chosen to produce a polymer dictate the properties of the polymer[64,65] produced and polymers comprising a single monomer type usually exhibit a linear chain. On the other hand, if the polymerization units comprise more than one monomer unit, i.e., oligomers, the result of its polymerization is a bottlebrush structure. Also called polymer brushes, they exhibit low friction and antifouling surfaces and have been explored to produce surfaces with these characteristics for industrial and biological systems.[65,64,69] Moreover, they can be very useful for TE in the creation of gliding surfaces, the aim of this section of this thesis.

Poly(ethylene glycol) (PEG) and an associated oligomer poly(ethylene glycol) methyl ether methacrylate (OEGMA), made of repeating PEG units modified with a methacrylate group, are of great interest for this work as they are known to be antifouling to both cell and protein adhesion and have been extensively explored for surface functionalization in industry and medicine.[70,71] This, together with the fact of these polymers being used in FDA approved devices, being biocompatible and excreted in urine, makes them good candidates for surface functionalization of tissue engineered scaffolds.[72] In this work, the oligomer OEGMA is used, as it has been successfully polymerized using ARGET ATRP in aqueous solution[62] and translated to polymerization from surfaces by Rachel Harrison et al 2015[47]. The scheme in Figure 3.1.4, adapted from Harrison *et al.* 2015[47] shows the ARGET ATRP polymerization process from a BiBB-initiated slab and from a BiBB-initiated fibre into bottle-brush functionalized PCL, as performed in this work.

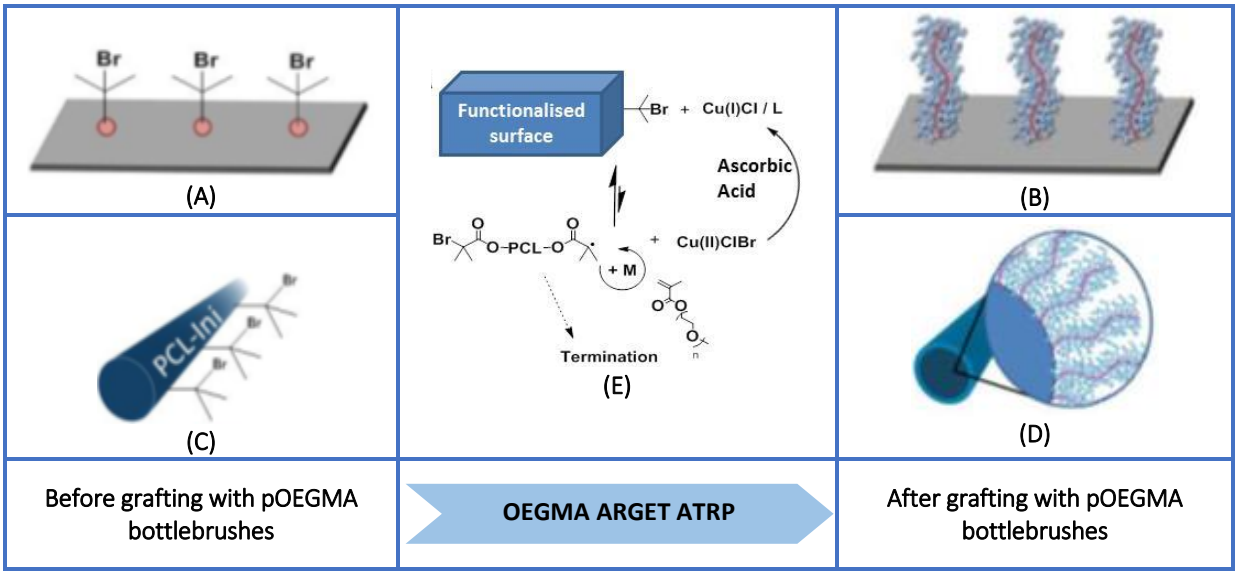

Figure 3.1.4 – Schematic of functionalised 2D PCL surfaces before (A) and after (B) grafting with pOEGMA bottlebrushes and of functionalised 3D electrospun fibres before (C) and after (D) grafting with pOEGMA bottle brushes. (E) Schematic of ARGET ATRP controlled radical polymerisation mechanism from surfaces.

In order to further prove the grafting of the pOEGMA on PCL surfaces, a biotinylated PEG monomer (chemical structure shown in Figure 3.1.5) was produced using Fmoc peptide synthesis and was copolymerized with OEGMA to produce p(OEGMA-co-biotin).

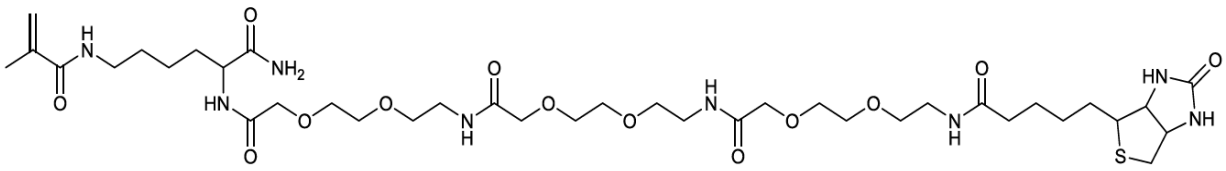

Figure 3.1.5 – Chemical structure of the biotinylated PEG monomer. From Harrison et al. 2015[47].

This PEG monomer comprises a lysine, a methacryloyl chloride group and three O2Oc groups (PEG units with amino acid functionality). The O2Oc are PEG units with amino acid functionality and were important to mimic the hydrophilicity and flexibility of the OEGMA monomer while also giving the biotin space to bind to the streptavidin without steric hindrance. The methacryloyl chloride was important to make the monomers more similar to the OEGMA ones, since they both share a methacrylate group.

To conclude the assessment of the p(OEGMA-co-biotin) on PCL fibres after melt electrospinning of the PCL-initiator (described in section 4.2.2) and post-polymerisation, the fibres were fluorescently labelled with streptavidin-fluorescein isothiocyanate (FITC) and the fibres were analysed using the fluorescence microscope, as streptavidin binds to biotin. The schematic representation of this step is shown in Figure 3.1.6.

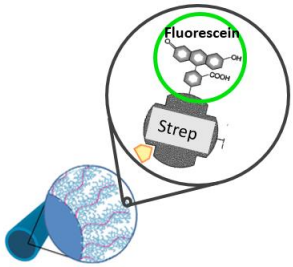

Figure 3.1.6 – Schematic representation of the FITC-streptavidin labelling of p(OEGMA-co-biotin).

3.2. Materials and methods

3.2.1. End functionalization of PCL with polymerization initiator

PCL-diol (50% w/w 45-80 kDa) was functionalized with the polymerization initiator BiBB using a protocol adapted from literature[47] to produce PCL-Ini (Figure 3.1.3).

Briefly, to produce 1 g of the PCL-Ini (17% (w/w) BiBB), 830 mg of a 50:50 45kDa:80kDa PCL blend (Sigma Aldrich) was diluted in 4 mL of anhydrous tetrahydrofuran (THF) in a glass vessel (7 mL) until complete dissolution. Afterwards, 170 mg of BiBB was added into the vessel and the reaction was let to react over night at room temperature.

Finally, the final reaction mixture was reduced through vacuum rotary evaporation and precipitated into cold diethyl ether (DEE). After three washes in DEE, the product was dried in a vacuum drier and storage at 4ºC.

3.2.2. Development of a biotinylated monomer for production of p(OEGMA-co-biotin)

A 0.30 mM scale of biotinylated PEG monomer was synthesized by manual Fmoc-SPPS, as described in Harrison *et al.* 2015, and using the same equipment as for the HA-BP synthesis. Common reagents to both synthesis were purchased from the same distributors, unless otherwise stated. Succinctly, after swelling of the resin with DCM, it was deprotected and coupled to Fmoc-Lys(Mtt)-OH (4 eq., 2h).

As for the remotion of the Mtt group, a solution of 1.5% (v/v) TFA in DCM was used to wash the resin (2x 15 min). The resin was further washed with DIPEA in DMF 1% (v/v) and DCM after which methacryloyl chloride (8 eq., 10 min) in DCM was coupled to the free amine. Three units of Fmoc-O2Oc-OH (2 eq., 3 h) were then coupled to the resin, followed by a biotin group after the final fmoc deprotection. All couplings were performed with HBTU (4 eq.) and DIPEA (8 eq.). The monomer was cleaved from the resin with a cocktail of TFA / triisopropyl silane / H2O (95/2.5/2.5 v/v/v, 2 h), precipitated in DEE and purified by HPLC (C18 column, H2O / acetonitrile gradient).

3.2.3.OEGMA polymerization in solution and from 2D and 3D PCL-initiated structures

The protocol followed, adapted from Harrison *et. al* 2015[47], consists in three major procedures: removal of inhibitors from the OEGMA monomer, ARGET ATRP reaction and termination of the reaction.

The first step was performed by creating a column with a syringe, filled 1/20 with cotton wool (to act as a filter), 7/20 with basic aluminium oxide purchased from Sigma Aldrich and 8/20 with inhibitor removal beads. Poly(ethylene glycol) monomethyl ether monomethacrylate (OEGMA) purchased from Polysciences (Germany) with a M_n of the poly(ethylene glycol) unit of 400 Da was then allowed to gravity filter though the column and aliquots were frozen at -20^{o}C until use.

The ARGET ATRP reaction was performed in a glass flask (the reaction vessel) on ice, OEGMA (227 mg, 0.7 mmol, Polysciences, Germany), copper (II) chloride ($Cu(II)Cl_2$, 0.42 mg, 0.0047 mmol), tris[(2-pyridyl)methyl]amine (TPMA, 1.37 mg, 0.0047 mmol), and ethyl α-bromoisobutyrate (EBiB, 0.92 mg, 0.0047 mmol) were added in 2 mL of 50% (v/v) isopropyl alcohol (IPA) aqueous solution. The vessel was then sealed and degassed with nitrogen for 30 min. An ascorbic acid solution (AscA 0.08 mg, 0.00047 mmol) was also degassed with nitrogen for 30 min and then added to the reaction with a syringe. The reactor was covered in aluminium foil, placed into a pre-warmed water bath at 31ºC and let react for 2h. After this time, the reaction was stopped by exposing the reaction to oxygen and confirmation of polymerization was assessed by size exclusion chromatography (SEC) using a 1260 Infinity Binary LC System (Agilent Technologies, UK).

3.2.4.Assessment of the p(OEGMA-co-biotin) polymer brushes on PCL-initiated printed scaffolds

The FITC-streptavidin protocol followed was adapted from Harrison *et. al* 2015[47] and started by the blocking of the p(OEGMA-co-biotin) polymerized scaffolds with a 1% (w/w) bovine serum albumin (BSA) and 0.1% (w/v) tween 20 in PBS solution for 30 minutes. Afterwards, the samples were stained for 15 minutes with fluorescein-streptavidin diluted to 1 µg/mL in 1% (w/w) BSA in PBS at pH 8.4 and washed three times with PBS. The samples were imaged on a fluorescence microscope Axio Imager M2 (Zeiss).

3.3. Results and discussion

3.3.1. Development of a biotinylated monomer for production of p(OEGMA-co-biotin)

The biotinylated PEG monomer was successfully synthesized and characterized with electrospray ionization mass spectroscopy (ESI-MS) and proton nuclear magnetic resonance (^{1}H-NMR), present in Appendix 6.3. The expected molecular was 876 kDa[55] and the ESI-MS proved the same value, confirming the production of this monomer unit.

3.3.2. ARGET ATRP polymerization

ARGET ATRP polymerization in solution and polymer brush grafting from PCL-initiated surfaces and from electrospun fibers were performed using the optimized reaction conditions found in Harrison *et al. 2015*[47]. A typical polymerization (**Error! Reference source not found.**(A) – (C)) achieved approximately M_n = 30 000, M_w = 40 000 and ispersity 1.2-1.3 (Table 3.3.1).

The graphics shown in result from the treatment of the data obtained by SEC, shown in Appendix 6.4, where the retention time, t_R is plotted against the MW and the refractive index, RI. Firstly, the calibration curve, that correlates t_R with $\log(\mathrm{MW})$ in a cubic equation of the type $\log(\mathrm{MW}) = \mathrm{a}t_R{}^3 + \mathrm{b}t_R{}^2 + \mathrm{b}t_R + \mathrm{c}$ ($\forall\, t_R :: 4.3677 < t_R < 7{,}6777$), was used to calculate the MW for each retention time point. The resulting MW was then plotted against the RI, the signal that shows the relative quantity of each molecular weight species. In the graphics shown in Appendix 6.4, the raw data, high molecular species are eluted from the column first, the polymer corresponds to the earlier peak and the monomer to the later peak. The treatment of the raw data aims at presenting the data in a more informative manner with the monomer (M) peak at the low molecular weight and the polymer (P) at the higher molecular weight.

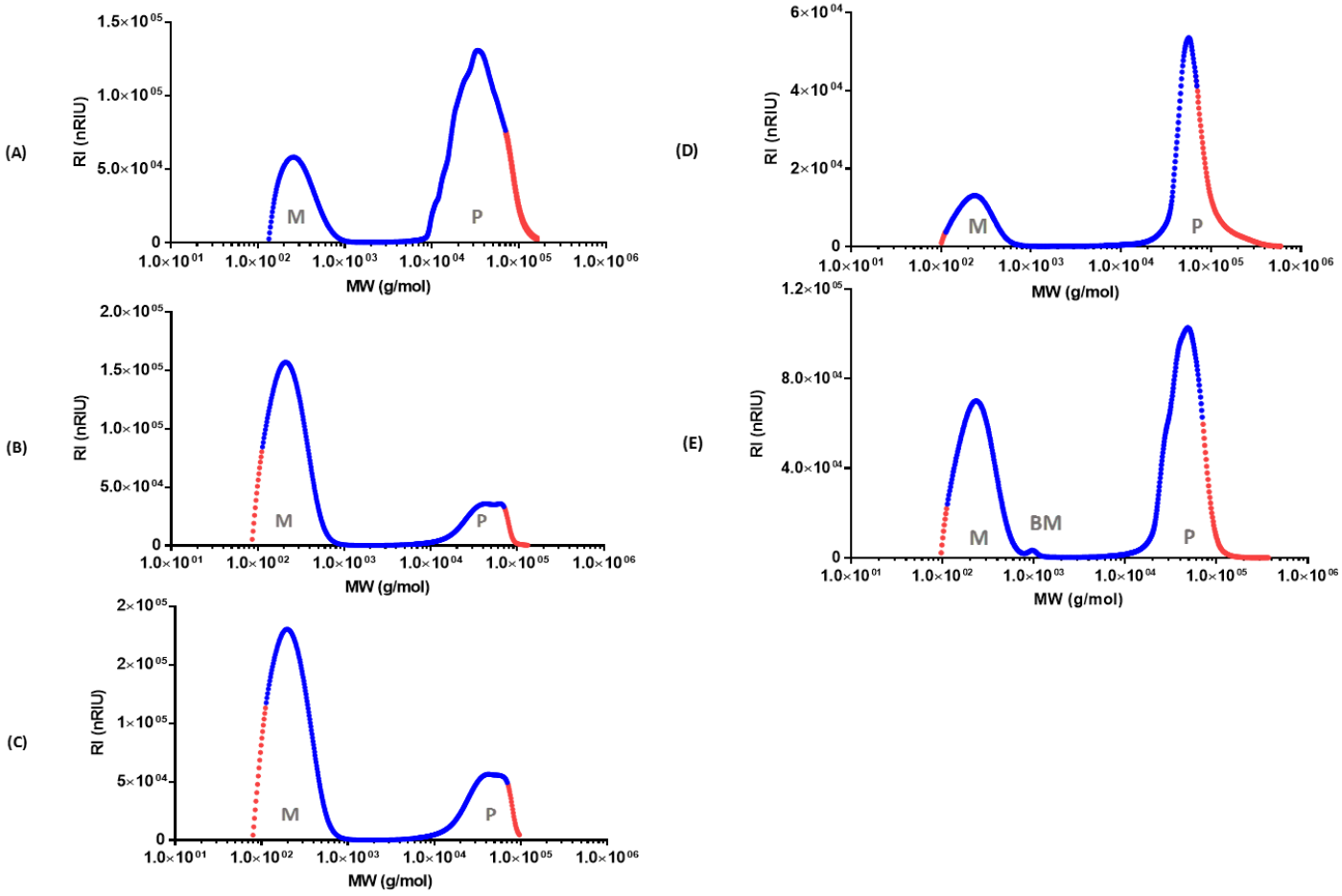

Figure 3.3.1 – SEC chromatograms of OEGMA 2 hour (except for (D), 24h) polymerization into pOEGMA by ARGET ATRP. (A) solution polymerization. (B) pOEGMA grafting from a PCL-initiated surface. (C) pOEGMA grafting from PCL-initiated electrospun fibers. (D) solution polymerization 24 hour assay. (E) p(OEGMA-co-biotin) grafting from PCL-initiated electrospun fibers. Blue points represent the molecular weights within the calibration range, and red points represent extrapolated estimates beyond the calibration. Peaks are identified as OEGMA monomer (M), pOEGMA brushes (P) and unreacted biotinylated monomer (BM).

Table 3.3.1 – Estimation of average molar masses (M_n, M_w) and PD.

Sample	Peaks	M_n (g/mol)	M_w (g/mol)	PD
(A) pOEGMA Solution Polymerisation (2h)	M	208	253	1.22
	P	**32525**	**40054**	**1.23**
(B) pOEGMA Grafting from PCL-BiBB Surface (2h)	M	209	254	1.22
	P	**31018**	**40671**	**1.31**
(C) pOEGMA Grafting from PCL-BiBB Fibres (2h)	M	199	247	1.18
	P	**28698**	**39538**	**1.24**
(D) pOEGMA Solution Polymerisation (24h)	M	231	273	1.18
	P	**53025**	**67376**	**1.27**
(E) p(OEGMA-co-biotin) Grafting from PCL-BiBB Fibres(2h)	M	227	268	1.18
	BM	961	972	1.01
	P	**38173**	**45608**	**1.20**

From Table 3.3.1, where $1.00 < M_w/M_n < 1.31$, it is possible to conclude that the reaction ran in a controlled manner, as PD < 1.5.

A 24-hour polymerization was performed in order to determine if the presence of residual monomer registered by SEC after the polymerization reaction was time-dependent or if it was caused by the contamination of the reaction vessel with small quantities of oxygen. As the graphic in (D) shows a monomer peak in the end of the 24 hours, one can conclude that probably the presence of oxygen maybe leading to the incomplete conversion of the reaction and that the presence of monomer after polymerization is independent from time. M_w and M_n showed higher values, as the polymerization time was increased. However, as M_n varies linearly with time of reaction, it would be expected higher value for this molecular weight. After polymerization overnight, the magnetic stir bar had stopped due to the increase in viscosity. The vessel showed two phases and only the liquid phase free polymer was analysed, hence the lower molecular weight obtained.

Also, the addition of the produced biotinylated PEG monomer to copolymerize into p(OEGMA-co-biotin) (graphic in (E)) shows a third peak when compared to the other graphics. This peak corresponds to an average molecular weight of 961 Da, in the range of the average molecular weight of the biotinylated PEG monomer. Moreover, the higher molecular weights when compared to the typical assays were expected as five per cent of the OEGMA monomer was substituted by the higher molecular weight PEG monomer.

Furthermore, to further prove the pOEGMA grafting on PCL-Ini scaffolds/surfaces, water droplets were placed on the top of PCL-Ini and PCL-pOEGMA surfaces. PCL-Ini fibers were hydrophobic, whereas PCL-pOEGMA were hydrophilic, as water droplets immediately wetted the surface. The schematic representation of this phenomena is presented in Figure 3.3.2.

Figure 3.3.2 – Scheme of the visualization of the wettability of PCL-ini surface (control) and of PCL-pOEGMA surface experiment performed in the laboratory. The first surface is shown to be hydrophobic, which is reversed by the addition of pOEGMA brushes.

This result helps to validate pOEGMA grafting, as PCL/PCL-Ini scaffold surfaces typically exhibit a contact angle of 113.5° ± 7.8°, which is reversed following pOEGMA grafting.[47]

3.3.3. Assessment of the p(OEGMA-co-biotin) polymer brushes on PCL-initiated printed scaffolds

In addition to the analysis of the free polymer in the reaction vessels and the hydrophobicity test, the presence of the polymer brushes were assessed using fluorescent labelling. The biotinylated PEG monomer was successfully polymerized together with OEGMA to produce p(OEGMA-co-biotin), as SEC results on section 3.3.2. The post-

polymerized fibres were then labelled with fluorescein-streptavidin and the images collected from fluorescent microscopy are displayed in Figure 3.3.3.

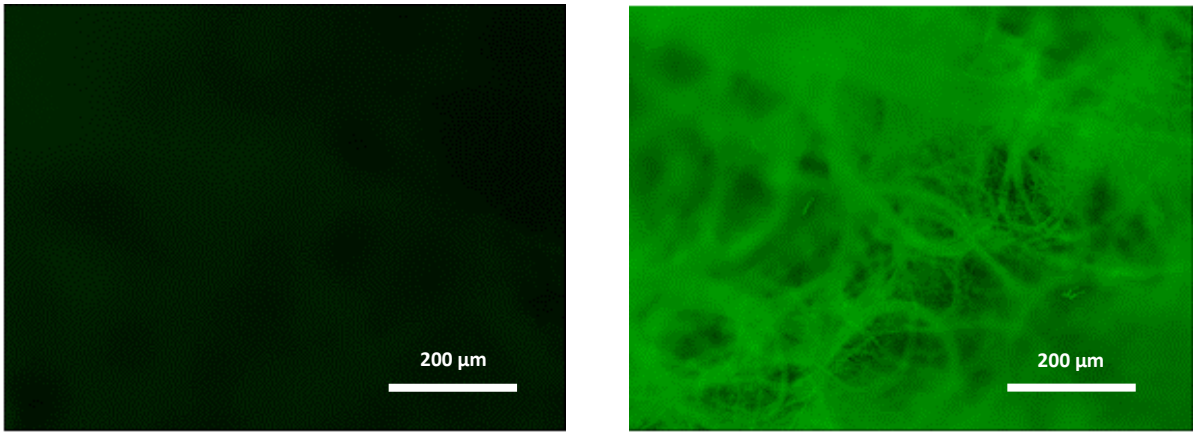

Figure 3.3.3 – Fluorescence micrographs of PCL-Ini (A) and PCL-p(OEGMA-co-biotin) FITC-streptavidin labelling (10x).

The image shown in Figure 3.3.3 (B), a section of the p(OEGMA-co-biotin) scaffold, show clear fluorescein conjugation when compared to the auto fluorescence of PCL-Ini scaffold shown in the same figure (A), which again corroborates the validation of the bottle-brush system.

In the same figure, it is worth noting the random fibre structure of the p(OEGMA-co-biotin) scaffold. After polymerizing the melt electrospun fibres with OEGMA and the biotinylated PEG monomer, the resulting polymerized scaffolds were washed three times in ethanol and sonicated for 30 seconds for removal of the free polymer formed in solution. This procedure was performed so that only polymer brushes grafted to the surface would be visualized after fluorescein labelling. Indeed, the combination of the washing with the sonication could have been in the origin of fibre deformation.

3.4. Conclusions

ARGET ATRP polymerization in solution, from surfaces and from 3D-electrospun scaffolds were successful, as determined by the SEC analysis of the free polymer in the reaction vessel. Also, the hydrophobicity test of PCL-Ini and PCL-pOEGMA and the fluorescent labelling of the biotinylated pOEGMA brushes corroborated the success in pOEGMA grafting.

4. Melt electrospinning writing (MEW) of functionalized-PCL for the production of 3D scaffolds

4.1. Introduction

4.1.1. Direct writing by way of melt electrospinning

The technique combines the cell-scale topographical features of traditional (solution) electrospinning with the spatial control and geometrical complexity of fused deposition modelling (FDM)[37,41], by melting a polymer rather than using a polymer solution. This solvent-free method can, therefore, avoid the volatility and toxicity issues associated with solvents.[73] Moreover, the higher viscosity and lower conductivity of melts when compared to solutions, leads to a drastic decrease of whipping and other instabilities during the production of the fibers with voltage applied.[74] This, associated to a computer controlled-stage, allows for the fabrication of controlled deposition of polymeric fibres, making melt electrospinning more similar to other additive manufacturing technologies, such as FDM and 3DP.

The main concern with this method, and common to AM techniques, relied in the lack of the sub-micron filaments that are important for controlling cellular key processes.[40,75,76] This limitation was surpassed by Hochleitner and Jungst 2015[39] by applying high electrical fields, low flow rates and small diameter spinnerets, achieving fibres with an average fibre diameter of 817 ± 165 nm after fifty double layers (2 single layers deposited perpendicularly) of stacking.

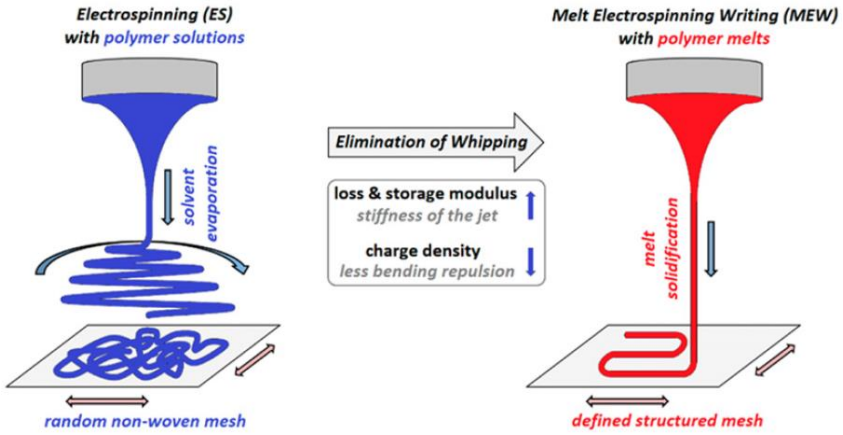

Figure 4.1.1 - Schematic of electrospinning and experimental configuration. (A) The use of a polymer melt instead of a polymer solution leads to a stabilized jet and a controlled direct writing approach for fibre deposition. From Brown et al. 2015.[40]

The diameter obtained for the fibres using ME for a specific material, as well as the fibre geometry deposition, can be controlled by manipulation of parameters such as spinneret diameter, pressure, voltage and collector distance and speed[41], as shown in

Figure 4.1.2. Also, in the same figure can be found other parameters affecting ME printing, such as charge interactions, temperature and polymer parameters. Regarding polymer parameters, they include electrical conductivity, molecular weight, tacticity and thermal properties.[73] For instance, fibre diameter increases with the increase of the molecular weight[77], pressure (melt flow rate, MFR); and it decreases with the increase of the collector plate speed and voltage applied.[78]

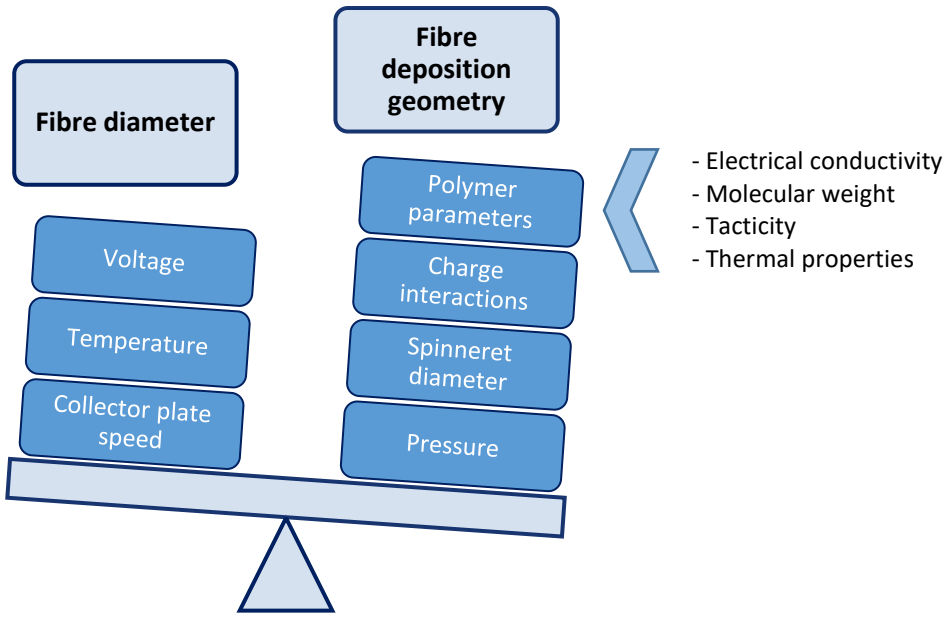

Figure 4.1.2 – Parameters affecting melt electrospun fiber diameter and deposition geometry.

In this work, the main parameters that were manipulated included extrusion pressure, temperature and collector speed. These parameters were manipulated in order to overtake the effect of functionalization of PCL with charged molecules in the control of fibre deposition.

Indeed, electronegative molecules, sulfur monoxide (SO) and sodium chloride (NaCl), have been shown to increase the Coulombic charge repulsions along the jet of material flowing out of the needle, therefore creating bending instabilities and whipping. [79]

Collector speed rates are important for both fibre diameter and their geometric deposition. The forces acting on the jet profile are influenced by the jet speed, S_J, when comparing to the collector speed, S_C. In Figure 4.1.3, these relationship on the geometry of fibre deposition is shown. Moreover, this figure shows four different cases for four different relative collector speeds. When the collector has no movement ($S_C = 0$) (1), the jet's path is straight with *compressive heel* close to the collector where buckling, i.e., bending and folding of the fibres, occurs. This leads to the coiling of the fibres. Between this situation and the following one (2), fibre deposition varies from a coiling geometry to a wave or straight deposition. In this second situation ($S_J = S_C$), the heel region in the jet is decreased to a balance between the tensile and compressive forces existent. For larger speeds of the collector plate when

comparing to the jet speeds (situations 3 and 4), the point of contact between the jet and the collector begins to *lag* behind the point directly below the spinneret and the jet acquires a concave profile, that becomes more pronounced with the increase of the collector speed.[80]

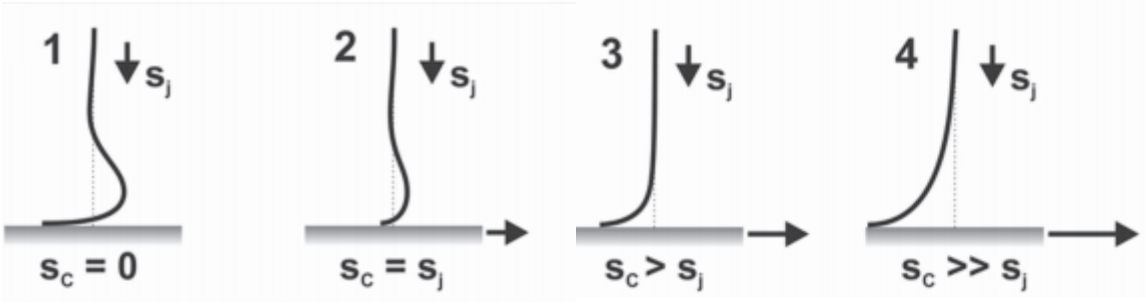

Figure 4.1.3 – Scheme showing the dependence of the ME jet profile with the relative speed of the collector, S_C, towards the speed of the jet, S_J. From Brown et al. 2011[41].

Kim *et al.*[81] have shown the volumetric flow rate, Q, to be the parameter affecting the most the average fibre diameter (AFD) between the temperature, diameter of the spinneret, the spinneret to collector distance (TCD) when ME of PLGA fibres. Conversely, Q can be related to the pressure applied by the Hagen-Poiseuille equation for laminar flow of a viscous fluid (Equation 1), where the pressure reduction, ΔP, is proportional to Q:

$$Q = \frac{\pi R^4}{8\eta L}\Delta P \qquad \textit{Equation 1}$$

Where Q is the flow rate of the fluid, R and L the radius and the length of the pipe, respectively, η the fluid viscosity. From this equation, one can conclude that by increasing the pressure reduction

Concerning the dependence of the flow with the temperature, for a low melting point polymer such as PCL, with relatively low M_w and low η_{melt}, the decrease in η_{melt} with increasing T_m can be described mathematically. At T_m that are more than 100 °C above T_g, as in the case of PCL (T_g = −60 ºC), the η_{mel}/T_m dependence shows close resemblance to an Arrhenius-type equation (Equation 2):

$$\eta_{melt} = A^{Ea/RT} \qquad \textit{Equation 2}$$

where A is a constant, Ea is the activation energy for viscous flow and R is the universal gas constant. When plotting ln η_{melt} against $1/T_m$, an approximate straight line with a slope of E/R is obtained. For polymers that satisfy the above criteria, this relationship usually covers a temperature range of approximately 50–150°C.[82]

4.1.2.Configuration of the melt electrospinning device

The system for ME was disposed as presented in Figure 4.1.4. The equipment was composed of a grounded and CAD-controlled collector, a heating system, an electrode connected to a high voltage source and an electro-pneumatic valve that allows the setting and readjustment of the pressure driving the material to flow from a syringe connected

to a needle. The heating system was comprised of two heating elements, one located around the barrel of the syringe and the other located around the needle.

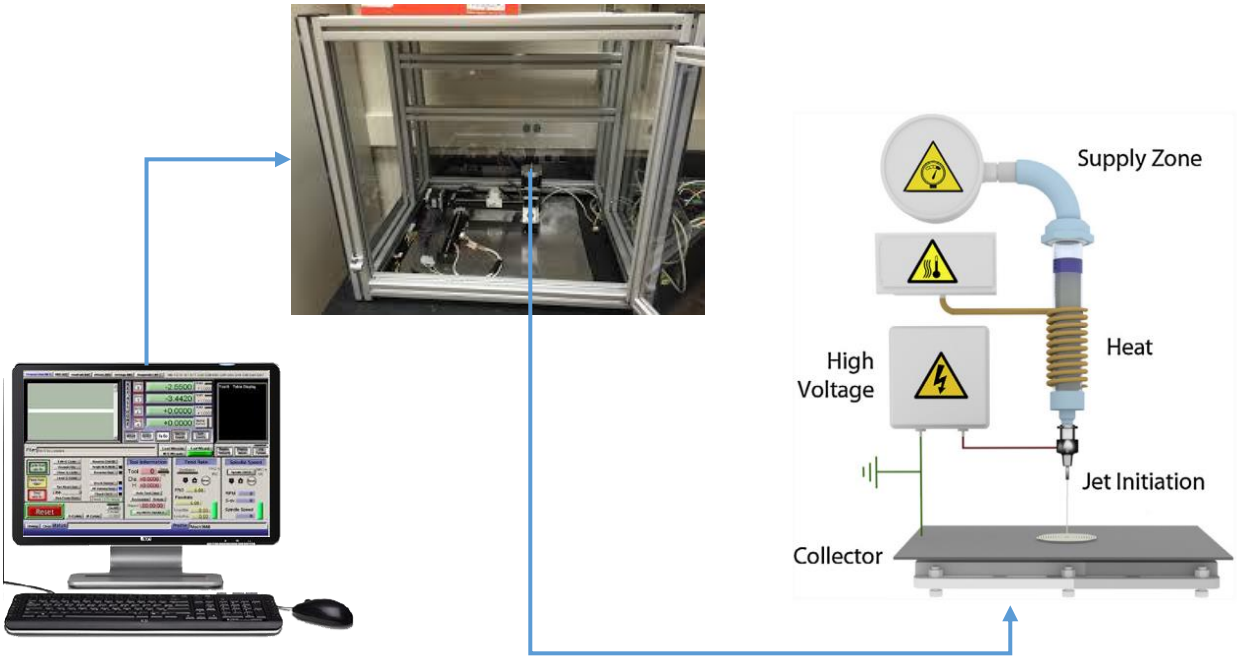

Figure 4.1.4 – Schematic representation of the ME printer setup used for the production of fibres. Adapted from Brown et al. 2015.[40]

4.1.3. Polycaprolactone for the production of the bulk scaffold

PCL is a resorbable polymer belonging to the family of aliphatic polyesters which is becoming an increasingly popular FDA-approved biomaterial to its good structural properties and processability.[16,39]

It was one of the first polymers to be synthesized, in the early 1930s, and is produced by the ring-opening polymerization of the cyclic monomer ε-caprolactone, as illustrated in Figure 4.1.5.The reaction is usually catalyzed by heat and stannous octoate.[83]

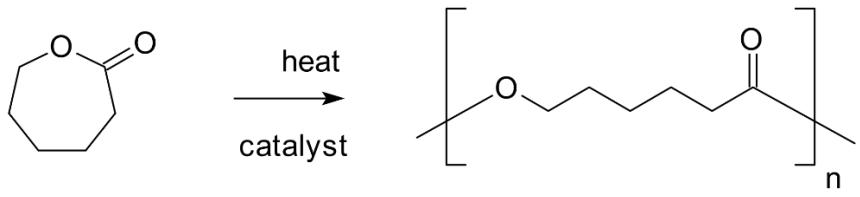

Figure 4.1.5 – Scheme of the polymerization reaction of ε-caprolactone towards poly(ε-caprolactone).

Although PCL was extensively used in biomaterials and drug-delivery fields during the resorbable-polymers boom between the 1970s and the 1980s, it was soon overwhelmed by the development of other resorbable polymers such as poly(lactide) and poly(glycolide). These polymers were preferred to PCL by the pharmaceutical industries as they

possessed lower resorption time needed for the release of encapsulated drug. As for the medical device industry, aiming at the replacement of metals for biodegradable implants, PCL did not have the mechanical properties for load bearing applications.[39]

The resurgence of PCL use was promoted by the development of the TE field and the realization that PCL possesses superior properties when compared to many other resorbable polymers concerning its rheological and viscoelastic properties. These make PCL easy to manufacture and manipulate, and hence, make it a good candidate for several fabrication techniques used in TE, such as solid free-form fabrication, 3D printing, fused deposition modelling, gas-foaming, solvent-casting and electrospinning, the fabrication technique explored in this work[39].

During this new boom of PCL as a biomaterial for TE, several groups extensively studied the mechanisms associated with its degradation *in vitro* and *in vivo*. From these, it was then concluded that PCL undergoes complete degradation in 2 to 4 years, depending on the starting molecular weight of the structure for implantation and the surface area to volume ratio, and that degradation time can be tailored by copolymerization with other lactones or glycolides/lactides. Furthermore, during *vivo* degradation studies, it was also concluded that PCL (as a homopolymer) undergoes a two-stage degradation process. The first stage consists in the non-enzymatic hydrolytic cleavage of ester groups, accurately modeled by *in vitro* hydrolysis at 40ºC, obeying first-order kinetics. The kinetics of hydrolysis depend on the molecular weight of PCL, as longer chain lengths resulting in a greater number of ester bonds to be cleaved in order to release water-soluble monomers/oligomers, increasing the degradation time.[39] The second stage consists in the intracellular degradation of the polymer, which was shown by the observation of PCL ≤ 3 kDa within macrophages and within fibroblasts. This stage starts when the polymer reaches low molecular weights and is more highly crystalline, being by then completely resorbed and degraded by intracellular mechanisms.[84]

Other property that makes PCL a preferred biomaterial for TE is its biocompatibility. Indeed, several studies have been performed in order to prove this property for both PCL and its composites. For instance, Hutmacher and co-workers have tested short-term – 15 weeks – and long-term – 2 years – PCL biocompatibility in rabbit and rat (calvarial critical-sized) models, reaching the conclusion that bone defects implanted with both PCL and PCL-TCP scaffolds showed an improved healing when compared with empty defects.[85,86,87,88]

4.2. Materials and methods

4.2.1. Preparation of the PCL blends for melt electrospinning

45 kDa (M_n = 45 000) and 80 kDa (M_n = 80 000) poly-ε-caprolactone (PCL) were purchased from SigmaAldrich Co. LLC. In order to print the PCL fibers, a blend 50/50 (w/w) was made by dissolution of both MW PCL in chloroform (20% w/v), purchased also from SigmaAldrich, in a glass flask under moderate stirring. After complete dissolution (approximately 1h), the solvent was removed under nitrogen and vacuum drying. The blend was then loaded into a syringe and heated (85 °C, 5 mbar) before processing by MEW.

4.2.2. Production of non-functionalized and functionalized PCL fibres by MEW

PCL fibres were produced using a direct writing melt electrospinner engineered by the Hutmacher Laboratory (Queensland University of Technology, Australia). The machine is described in section 4.1.2.
The movement of the stage was controlled using CNC software Mach3 Mill (Arsoft), which controls the motion of two stepper motors by processing a G-code program.

4.2.3. Optimization of the diameter and geometry deposition of fibres by MEW

For this optimization, five different pressures (0.12-0.30 MPa) and five different collector plate speeds (500-1500 mm/min) were tested and the other parameters (temperature, T, and high voltage, HV) were kept constant (T = 75 °C, HV = 8 kV). In order to perform these tests in an efficient and uniform way, a G-code (Appendix 6.5.1) comprising five collector plate speeds was created and run for each pressure value. As shown in Figure 4.2.1, the G-code was designed in order to print in two distinct areas: a stabilization area (A) and a testing area (B). As the melt electrospinner starts printing with a new condition, the equipment needs time to reach stationary phase and print uniform fibers. Therefore, the program starts with the stabilization of the fibers by printing them in 80 passes in a part of the collector plate and then moves to the printing area to print in 8 passes in the testing area. These last fibers were the ones imaged and measured recurring to the fluorescence microscope (FM).

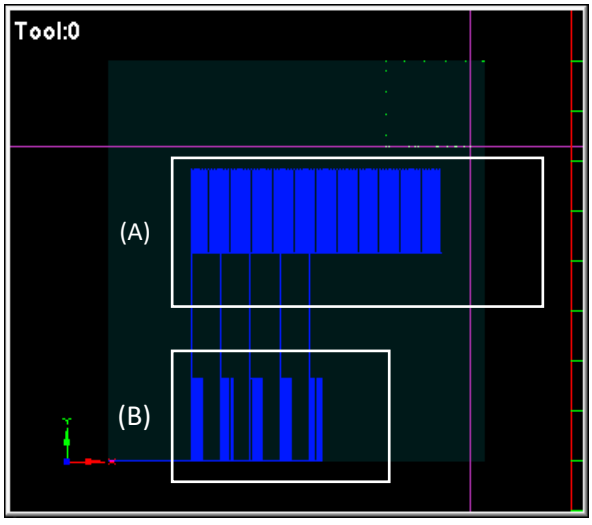

Figure 4.2.1 – Schematic representation of the collector plate shown in the window of the CNC software Mach3, after opening the G-code.

4.2.4. Production of non-functionalized and functionalized PCL scaffolds by MEW

In order to print 3x3 cm orthogonal grid scaffolds with 500 µm fibre spacing and 60 layers the G-code presented in Appendix 6.5.2 was written.

4.3. Results and discussion

The fabrication of PCL fibers and scaffolds was successful after optimization of parameters such as temperature, pressure and voltage. The first step consisted in printing 45 kDa PCL, in order to understand the phenomena associated with the deposition of several layers of fibers on the collector plate. After end-functionalizing 14 kDa PCL with the decorating peptides (PCL-HA-BP and PCL-cRGDS) and the polymerization initiator (PCL-Ini), 17% PCL-Ini, 5% PCL-cRGDS and 5% PCL-HA-BP in 50% 45-80 kDa PCL blends were produced and their printing into geometrically-controlled scaffolds was performed and optimized.

4.3.1. 45 kDa PCL Melt Electrospinning printing

The first printing assays were performed using 45 kDa PCL and consisted in a 3x3 cm, 60-layered scaffold. Figure 4.3.1 shows the bottom view (in (A)).

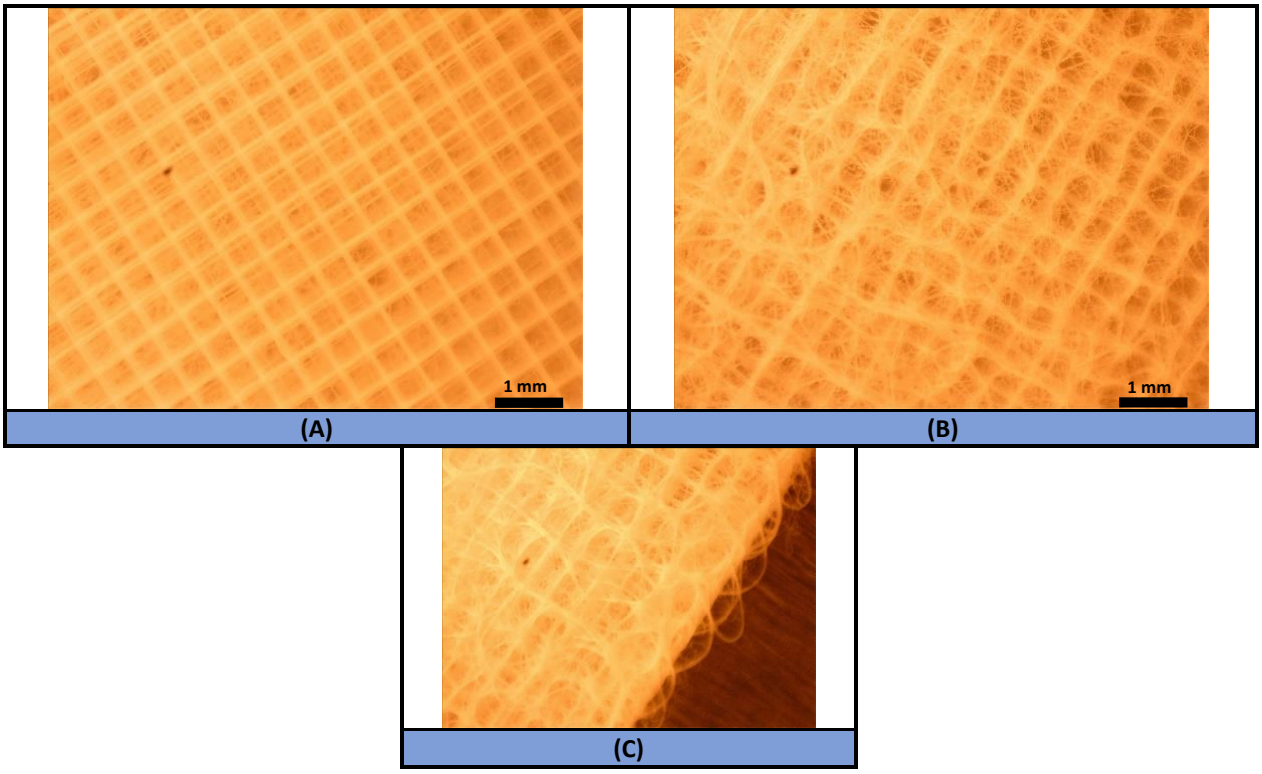

Figure 4.3.1 – 60 double-layered melt electrospun scaffold of 45 kDa PCL. (A) Bottom view, (B) top view, (C) detail of an edge of the scaffold. Parameters used: Ttube = Tring = 75 °C, HV = 7 kV, P = 0.12 MPa, PS=0.50 mm.

4.3.2.50% (w/w) 45-80 kDa PCL Melt Electrospinning

This blend was the one chosen for all peptide and initiator blends printing, due to its consistent printability, as shown in Figure 4.3.2.

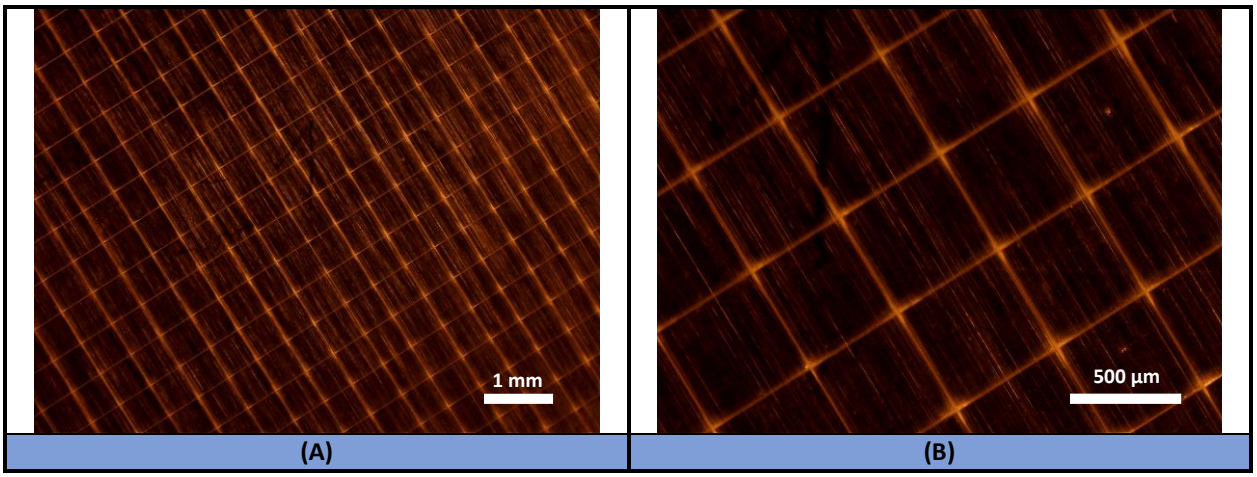

Figure 4.3.2 – USB microscope images of a 50% (w/w) 45-80 kDa PCL double-layered scaffold. Printing parameters: Tring = Ttube = 70°C, P = 0.120 MPa, speed = 1000 mm/min, HV = 8kV, PS=0.50 mm.

4.3.3.50% (w/w) 45-80 kDa PCL-Initiated (17% EBiBB) Melt Electrospinning printing

This printing aimed at producing fibers with the polymerization initiator, BiBB, on its surface. To our knowledge, this is the first instance of end-functionalized polymers processed by ME. The 17% (w/w) concentration value of BiBB resulted from an optimization work from *Harrison et al. 2015.*[47] The melt electrospinner was set up with the cathode at the spinneret, i.e., the polymer melt was conveyed with a positive charge on its surface. Simultaneously, the alkyl-bromide group comprised within BiBB can become electronegative due to its polarity and, promoted by electrostatic attraction, can migrate through the polymer solution, resulting in surface presentation of the initiating groups.[89] The PCL-ini was subsequently electrospun in combination with the 45-80 kDa PCL blend to form functionalized fibrous scaffolds which were photographed by an USB microscope, as shown in Figure 4.3.3 and Figure 4.3.4.

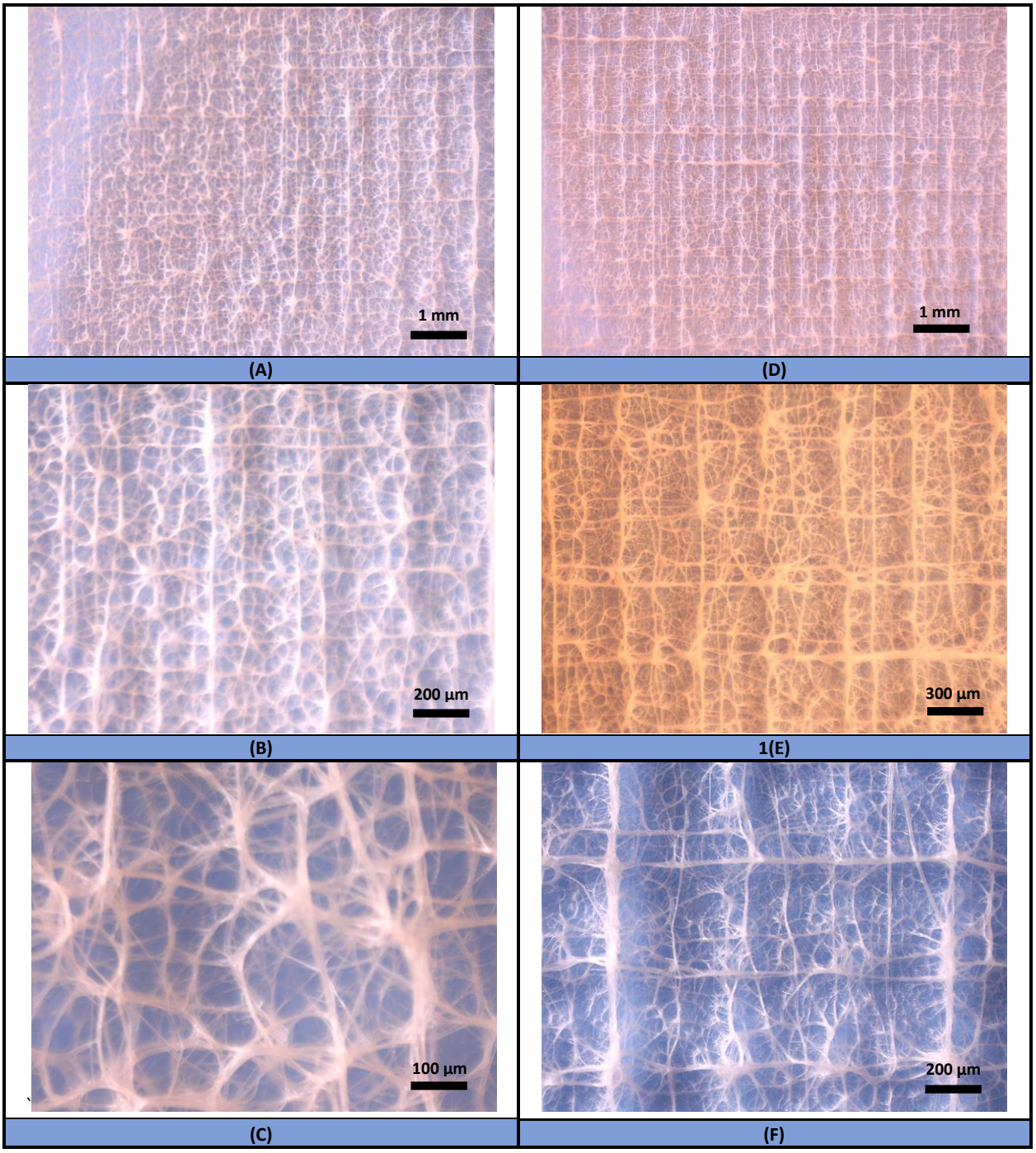

Figure 4.3.3 - USB microscope images of PCL-Ini 30 double-layered scaffolds with 17% (w/w) BiBB. Printing parameters: Tring = Ttube = 95°C, P = 0.250 MPa, speed = 1000 mm/min, (A)-(C) HV = 8kV, PS=0.50 mm. (D)-(F) HV=7kV, PS=0.25 mm.

After reaching conditions that allowed the uniform flow of material through the spinneret, a 3x3 cm scaffold was printed as shown in Figure 4.3.3 (A)-(C). These images show that the fibres were not deposited in an organized pattern such as presented in figure Figure 4.3.1, in spite of the larger pressure and temperature used (Figure 4.3.3 (A)-(C)). This can be due to the polarity of BiBB, which can result in instabilities during fibre production and deposition because of the use of the HV. In order to improve the printing pattern, and bearing in mind the polarity of BiBB, a lower

voltage was used, 7 kV, and the pore size was diminished to half, PS = 0.25 mm, resulting a new scaffold, shown in Figure 4.3.3 (D)-(F).

By comparing the fibres from images (A)-(C) in Figure 4.3.3 to the ones from images (D)-(F), this new printing conditions seem to be granting a slightly better level organization to the scaffolds, as it can be distinguished a more organized macrostructure with the perpendicular deposition of fibres and a more randomized microstructure. These scaffolds comprises, then, several degrees of complexity such as the ones needed to mimic the *in vivo* histology of tissues.

In an attempt to better improve the control of fibre deposition in 17% BiBB scaffolds, and as with larger S_C values the fibres suffer a greater extension before solidifying, the speed of the collector plate was increased from 1000 to 1400 mm/min, the temperature was decreased from $T_{ring} = T_{tube} = 95°C$ to $T_{ring} = 90°C$, $T_{tube} = 85°C$ and the PS was increased to 0.5 mm so as to produce different functionalized PCL scaffolds with the most similar geometry for reliable cell assays regarding functionalization and not geometry. The resulting scaffold is shown in Figure 4.3.4.

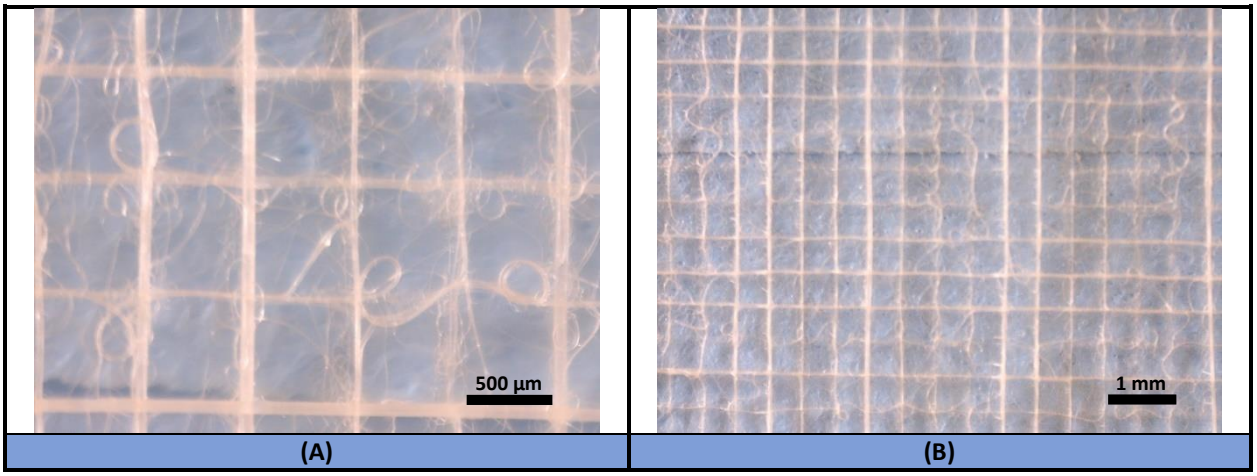

Figure 4.3.4 – USB microscope images of PCL-Ini 10 double-layered scaffolds with 17% (w/w) BiBB. Printing parameters: Tring = 90°C, Ttube = 85°C, P = 0.250 MPa, speed = 1400 mm/min, HV=7kV, PS=0.50 mm.

By analyzing the images (Figure 4.3.4) one can argue that these new conditions produce more controlled patterns, such as the ones shown in Figure 4.3.1 and Figure 4.3.2. One can also observe that this new scaffold seems to maintain several degrees of complexity as it can be seen larger fibers deposited perpendicularly in a mesh and smaller randomized fibers.

4.3.4.45/80 kDa (50% w/w) PCL-HA-BP (5% w/w) Melt Electrospinning printing

This printing aimed at producing fibers functionalized with the hyaluronic acid binding peptide (HA-BP). The images and the parameters found to print this 5% HA-BP in PCL blend are shown in Figure 4.3.5.

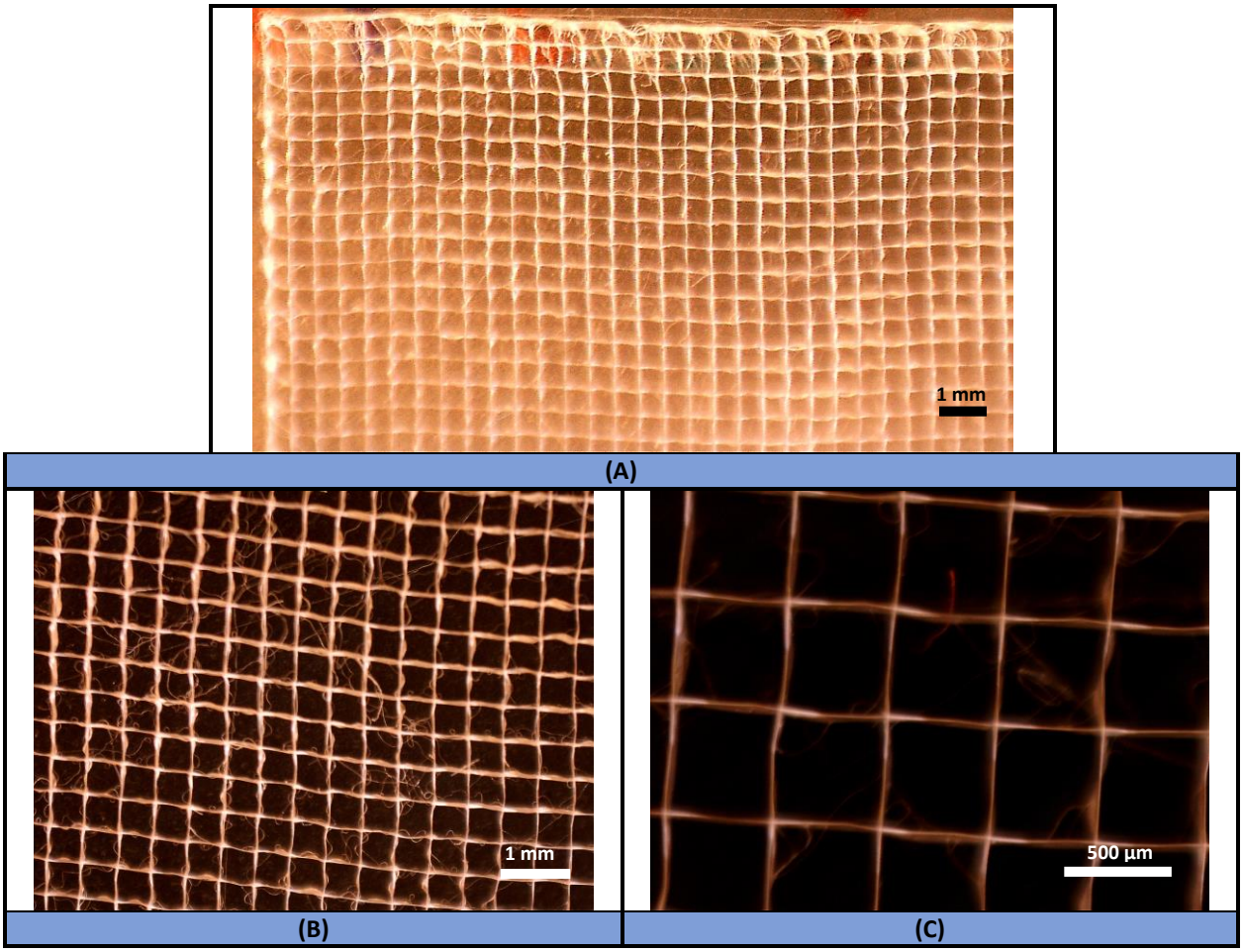

Figure 4.3.5 - USB microscope images of 30 double-layered scaffolds with 5% HA-BP in PCL. Printing parameters: Tring = 80 °C 85°C, P = 0.250 MPa, speed = 850 mm/min, HV=8kV, PS=0.50 mm.

This functionalized PCL was found to be the easiest to print. This is advantageous, as the scaffolds for cartilage regeneration benefit from smaller pore sizes, between 150 and 250 µm[90]. Since this 500 µm spaced scaffold displays a consistent printability and since diminishing the pore size of a scaffold leads to the increase in the electric interactions between the molten filament being printed and the already printed fibres, which affects the control of fibre deposition, this blend shows potential to produce smaller pore-sized scaffolds as the ones needed for cartilage engineering.

4.3.5.45/80 kDa (50% w/w) PCL-cRGDS (5% w/w) Melt Electrospinning printing

This printing aimed at producing fibres functionalized with a cyclized version of the canonical cell adhesion motif (RGDS), cRGDS.

It has been demonstrated for solution electrospinning the fibre's surface enrichment of the RGDS motif when the spinneret is positive.[91] The same was demonstrated by *Harrison et al. 2015*[47] using the same electrospinning set up for the cRGDS. Although ME recurs to polymer melts rather than polymer solutions, the polarity set up of the electrospinning device used in this work is the same as the ones aforementioned, despite the larger strength of the

electric field used in ME, 7 kV/10 mm, when compared to the one used for SE, 16 kV/100 mm. Hence, it was expected in this work that the cRGDS motif would be disposed on the surface of the PCL fibres. This is further validated with the fluorescent labelling of PCL-cRGDS, in section 2.3.2.

However, in spite of using the same polarity configuration as the previous referred works for this melt electrospinning device, it was not possible to succeed in producing controlled fibre patterns with cRGDS-enriched PCL as in the other functionalized PCL blends.

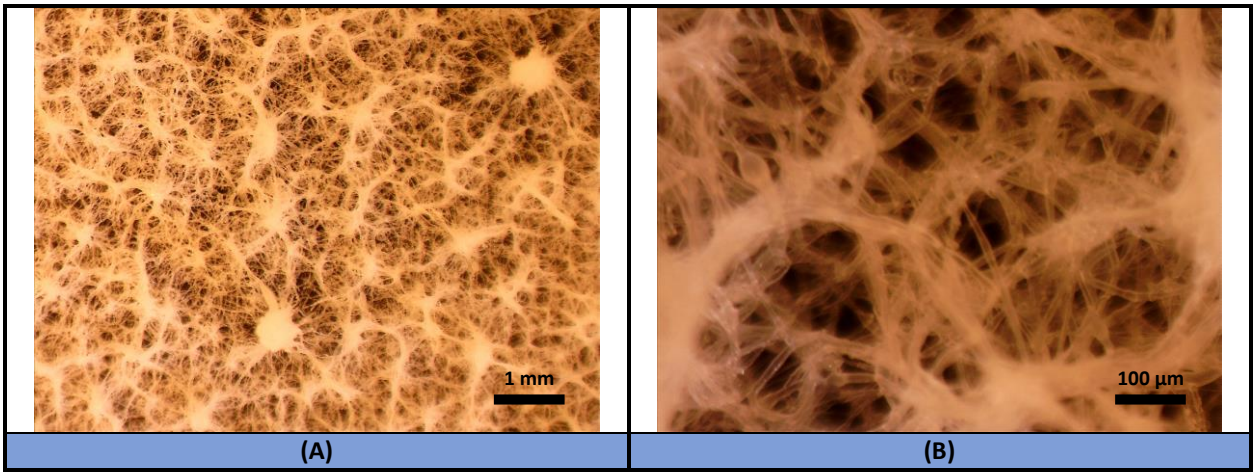

Figure 4.3.6 - USB microscope images of PCL with 5% (w/w) cRGDS. Printing parameters: Tring = 90°C, Ttube = 85°C, P = 0.250 MPa, speed = 1400 mm/min, HV=7kV, PS=0.50 mm.

Indeed, the printing of 5% cRGDS in PCL was attempted several times using pressures 0.20-0.30 MPa, HV 7-8 kV, speeds 850-1000 mm/min and temperatures ranging from 80 to 110°C. The PS was kept at 0.50 mm so as to avoid the effect of scaffold geometry in cell assays.

During the printing process for this functionalized PCL, it was observed that the fibres produced weren't continuous and uniform. As a matter of fact, the flow coming out from the spinneret was frequently stopped by what it seemed to be small crystals, probably insoluble peptide, that were clogging the needle. For this reason, the speed of the collector plate could not be increased above 1000 mm/min in order to straighten the fibres, as this would only result in the heterogeneous printing of this blend.

Several attempts were made aiming at the dissolution of the crystals, namely the sonication of the PCL blend dissolved in chloroform. Another possible solution would be the complete re-dissolution of the blend in chloroform, followed by a filtration in order to remove the crystals, task that wasn't performed due to restrictions in time.

4.3.6. Melt electrospun fibre optimization

To my knowledge, although there is an optimization for the AFD of 50 kDa PCL, there is no optimized standard operating procedure (SOP) that correlates the conditions used in ME with the resulting geometry deposition of fibres neither with their resulting diameter for this 50% 45-80 kDa PCL blend, the chosen for PCL functionalization. This

way, with the purpose of creating a general protocol for the production of scaffolds with tailorable of both fibre geometry deposition and fibre diameter, the protocol described in section 4.2.3 was followed. After collecting the resulting 50% (w/w) 45-80 kDa PCL fibres, the samples were imaged using the bright field of the FM. For each amplification, two photographs were taken and the 10x was used to understand the geometry of fibres deposition and 40x was used for the measurement of the fibre diameters, for more accurate results. The photographs taken are presented in Figure 4.3.7. The geometry of fibre deposition was also analysed and is presented in Table 4.3.1.

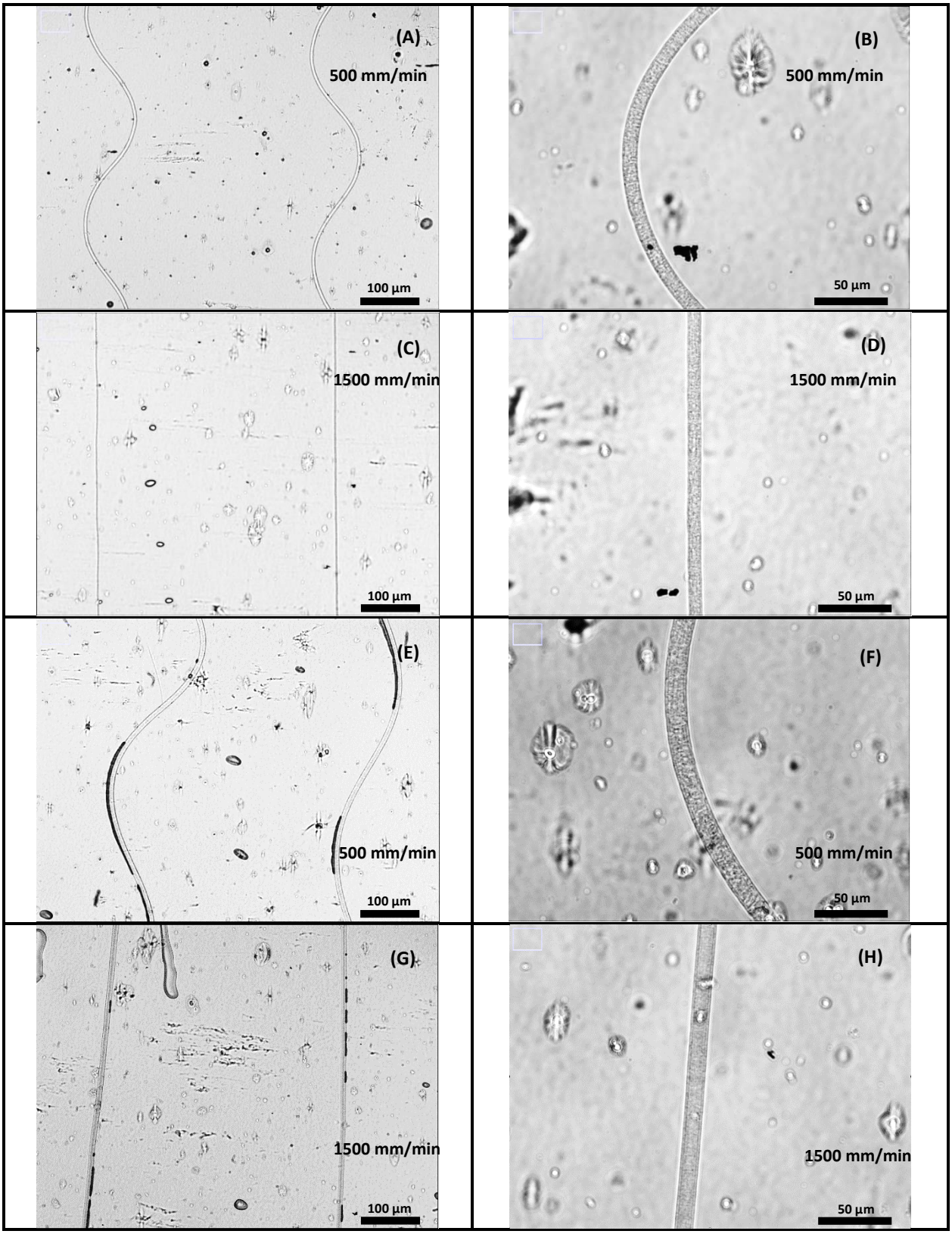

Figure 4.3.7 – FM photographs of single layer printed for 0.12 MPa and 500 mm/min: (A) 10x, (B) 40 x; and 1500 mm/min: (C) 10x, (D) 40 x. 0.30 MPa and 500 mm/min: (E) 10x, (F) 40 x; and 1500 mm/min: (G) 10x; (H) 40 x.

By analysing Figure 4.3.7, showing the four extreme conditions of pressure and collector plate speed used, one can conclude that for the highest collector speed rate, the fibres are deposited as straight lines (C,D,G,H) and, for the lowest values of this parameter, the fibres are deposited in an wave-like pattern, independently of the range of pressures tested. Moreover, Table 4.3.1 shows that for collector speeds rates between 500 and 750 mm/min the geometry for fibre deposition happens in a wave-like pattern and that for speeds between 1000 and 1500 mm/min the geometry turns into a linear fashion. In order to obtain coil-like patterns, the speeds applied should have been significantly lower.

Table 4.3.1 – Analysis of the fibre deposition geometry (linear, wave-like, coil-like)

	Speed (mm/min)				
	500	**750**	**1000**	**1250**	**1500**
Pressure (Mpa)	Linear/wave-like/coil-like				
0.12	Wave-like	Wave-like	Linear	Linear	Linear
0.15	Wave-like	Wave-like	Linear	Linear	Linear
0.18	Wave-like	Wave-like	Linear	Linear	Linear
0.21	Wave-like	Wave-like	Linear	Linear	Linear
0.24	Wave-like	Wave-like	Linear	Linear	Linear
0.27	Wave-like	Wave-like	Linear	Linear	Linear
0.30	Wave-like	Wave-like	Linear	Linear	Linear

Each assay was replicated independently in a total of three replicates and three diameter measurements were performed per assay. The total number of measurements for each condition was therefore six. An additional independent experiment and analysis could not be performed in the allotted time.

After measuring the diameter of the fibres, the AFD was estimated and the standard deviation for the six values for each condition was calculated. These results can be found in Table 4.3.2.

Table 4.3.2 – Average diameter measurements with the respective errors for each pressure and collector speed values. Cells are coloured with red gradients according to increases and decreases of values, in order to highlight the evolution of AFD with the two parameters in study.

	Speed (mm/min)					
	500		**1000**		**1500**	
Pressure (Mpa)	Average diameter ± σ (µm)					
0.12	8.4	± 0,6	6,9	± 0.4	5,7	± 0.1
0.15	9.3	± 0,5	7,2	± 0.2	7,7	± 0.3
0.18	9.9	± 0,9	8,7	± 0.1	7,7	± 0.5
0.21	11.2	± 0,4	8,8	± 0.3	8,5	± 0.4
0.24	11,9	± 0,9	9,0	± 0.3	10,1	± 1.3
0.27	11.5	± 1,1	11,2	± 0.3	9,3	± 0.3
0.30	12.1	± 0,4	11,3	± 0.2	10,7	± 0.5

The AFD values were then plotted in a graphic (Figure 4.3.8) against the pressure with their respective error for each set of collector speeds. A trend-line was added and the mathematical relationship between P and AFD (with the correlation coefficient, R) was found in the form of $AFD = mP + b$, where m and b are the slope of the curve and b the y-intercept value.

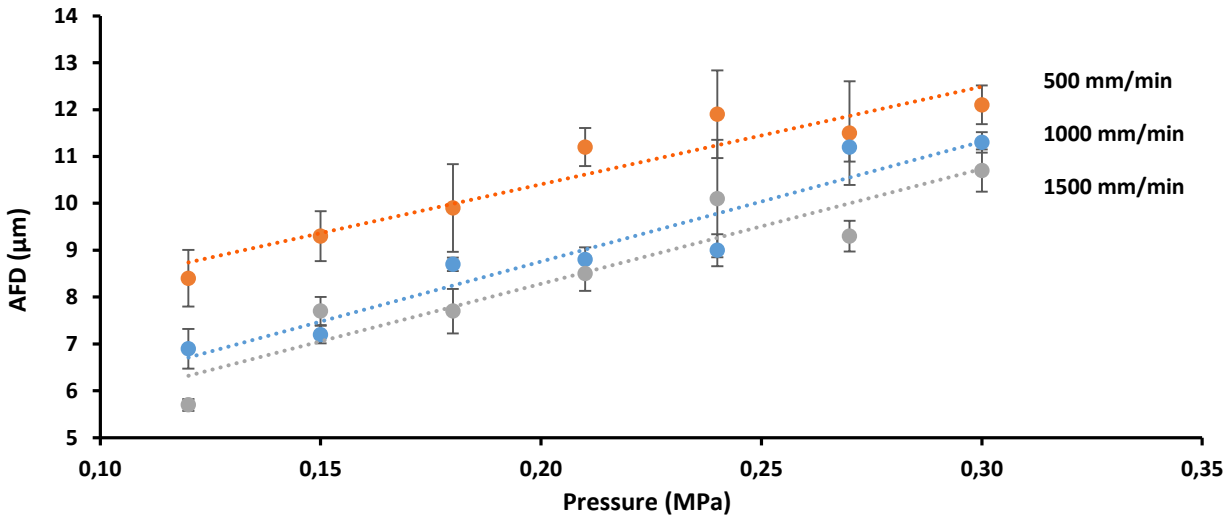

Figure 4.3.8 – Graphical representation of the influence of pressure and collector speed in the AFD of melt electrospun PCL fibres (T = 70 °C). After linearization of the data for each collector speed rate, AFD is given for 500 mm/min: $AFD_{500} = 20.8P + 6.2, R^2 = 0.90$; for 1000 mm/min: $AFD_{1000} = 25.8P + 3.6, R^2 = 0.92$ and for 1500 mm/min: $AFD_{1500} = 24.5P + 3.4, R^2 = 0.88$.

As expected[77], the biggest AFD value was achieved with the highest pressure and lowest collector speed rate. Conversely, the lowest AFD value was achieved with the lowest pressure and highest collector speed rate.

This optimization study is important to know what conditions to use regarding P and S_C to obtain a specific AFD in the production of scaffolds using the 50% 45/80 kDa PCL blend.

4.3.7. Melt electrospinning fibre deposition observations: degradation of PCL.

After a period of 3 to 4 weeks, the PCL blend 50% 45-80 kDa started to flow too much, bearing in mind the standard printing conditions used. Indeed, the printing pattern scheme shown in Figure 4.3.2 turned into the one shown in Figure 4.3.9, using the same conditions.

This phenomenon can be explained by the decrease of the molecular weight in the PCL blend, promoted by the thermodegradation of the material. Indeed, according to Fox and Loshaek[92], the basic equation relating viscosity at zero shear rate, η_0, to molecular weight for linear amorphous polymers was developed by Fox and Loshaek 1995[93] and is given by

$$\eta_0 = K\mathrm{M}_w{}^a \qquad \textit{Equation 3}$$

where K is a constant that depends on the polymer type, temperature and MW. One can conclude that with the decrease of the MW, the viscosity of the polymer at zero shear rate also decreases, which would cause the flow of the material through the needle to increase, and hence the wave and coil-like deposition of the fibres.

The thermodegradation of PCL was assessed by SEC analysis (Appendix 6.6) of the blend after printing for several weeks against a sample of the blend that hadn't been exposed to heat. By analysing Figure 6.6.1 and Figure 6.6.2 from Appendix 6.6 resulting from the SEC analysis, one can notice that molecular weights estimated are way lower (39131 Da for the blend before printing and 38182 Da for the blend after three to four weeks of printing) than the expected (50% 45-80 kDa = 62,5 kDa). One can also observe that the curves present in the figures aforementioned are up to the exclusion limit of the column in the area of larger molecular weights, which means the estimation values are not accurate. Furthermore, the column was calibrated with PEG, making this analysis a relative assessment, even within the curve. By making a rough comparison, the molecular weight for the initial blend is higher than for the blend after the heating periods, leading to the conclusion that there was PCL degradation.

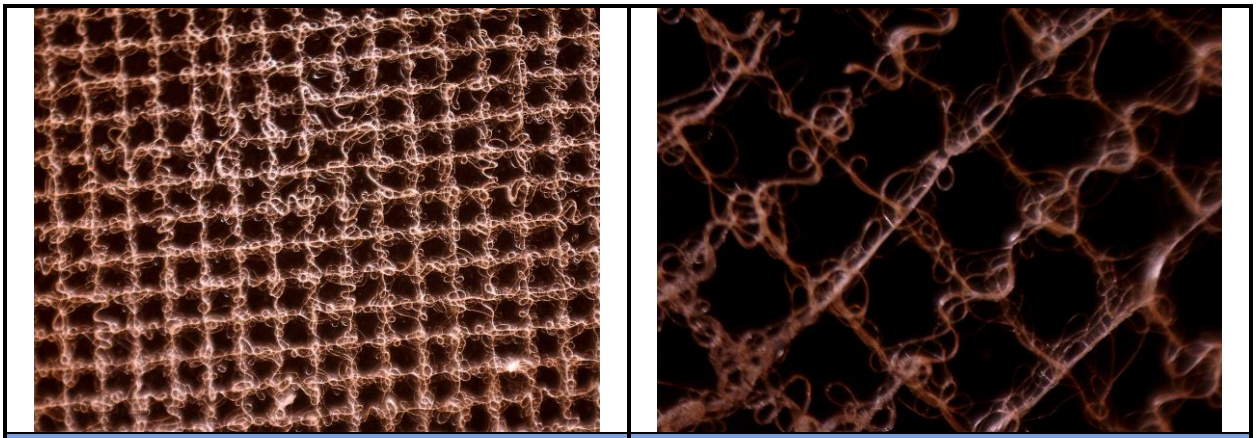

Figure 4.3.9 – USB microscope images of PCL-Ini 30 double-layered scaffolds with 5% (w/w) cRGDS. Printing parameters: Tring = 90°C, T_{tube} = 85°C, P = 0.250 MPa, speed = 1400 mm/min, HV=7kV, PS=0.50 mm.

For future blends, the printing time that each sample is submitted to, i.e. the time that the sample is submitted to temperatures above its melting point, should be accounted and summed until the printing is modified, so as to acknowledge the time a sample can resist to heat without substantial degradation.

4.4. Conclusions

The production of functionalized PCL scaffolds was successful for the 50% (w/w) 45-80 kDa PCL blend and for the end-functionalization of PCL with the polymerization initiator, BiBB, and for the PCL-conjugated HA-BP (5% (w/w)).

Continuous fibres and control over fibre deposition could not be reached in the case of cRGDS.

An optimization of the AFD was performed by manipulating the pressure and the collector speed rate applied in the ME process.

5. Final remarks and future directions

This work allowed for the confirmation that ME can be used for the production of geometrically-controlled fibres composed of biofunctionalized PCL with polymers and peptides, as has been proved before with SE.[47,48,91] Indeed, HA-BP and the canonical adhesion sequence cRGDS were successfully conjugated to PCL and located on the surface of PCL scaffolds after melt electrospinning. Also, PCL was successfully end-functionalized with the ARGET ATRP initiator, BiBB, and melt electrospun into scaffolds that were post-polymerized with ARGET ATRP on their surfaces.

Melt electrospinning technique was also optimized for the production of controlled diameter and geometry deposition of pure PCL fibres.

This work shows potential applications not only in osteochondral regeneration but in other fields of TE as the techniques used are versatile and capable of corresponding to the histological needs of different tissues.

Further work following this project would begin with the assessment of the cell adhesion and proliferation capacity of each functionalized scaffold with human mesenchymal stem cells (hMSCs), capable to differentiate into osteoblasts and chondrocytes, as cell adhesion is a key event for cell proliferation and differentiation, needed for regeneration of tissues.

Following this work, further cell assays should be performed to assess the differentiation capacity of each peptide-functionalized scaffold. This would hopefully show the enhanced differentiation of hMSCs into chondrocyte and osteoblastic lineages, in HA-BP and cRGDS functionalised scaffolds, respectively.

At the same with this experimental cell work, the printing of the functionalized blends should be further optimized to construct multi-layered scaffolds, which would be achieved by sequential ME of PCL-cRGDS (for the bone area), PCL-HA-BP (for the cartilage area) and PCL-p(OEGMA) (for the mobility of the joint). This way, a printing scheme as the one shown in Figure 5.1 could be attempted.

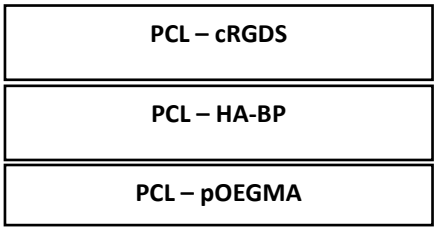

Figure 5.1 – Schematic representation of the idealised multi-layered osteochondral scaffold.

For accurate geometrical/histological recreation of osteochondral tissues, computed tomography from healthy patients could be used to obtain a CAD file with Materialise Mimics® software, for instance, and then this CAD file could be converted into G-code with Slic3r software, that would be used for ME printing of the osteochondral scaffold.

In sum, the systems here established will hopefully help to create efficient ways to ease the fabrication of porous scaffolds with appropriate biomimetic cues for osteochondral regeneration.

6. List of appendixes

6.1. HA – BP characterization

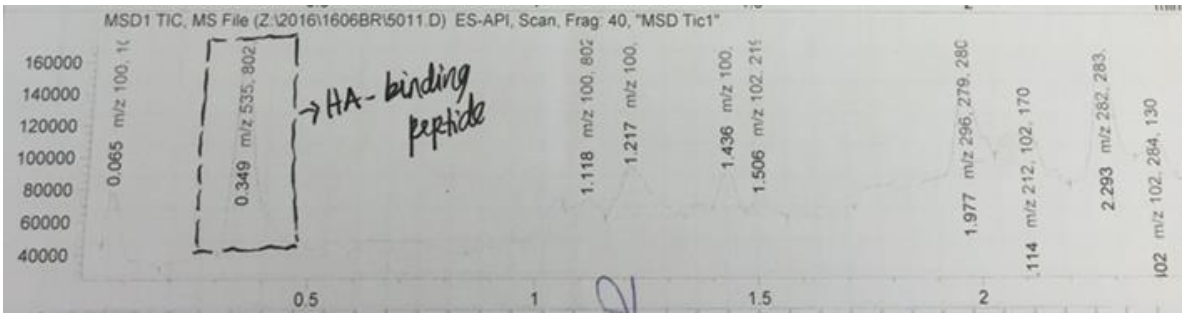

Figure 6.1.1 – ESI-MS mass spectrum of the HA – BP.

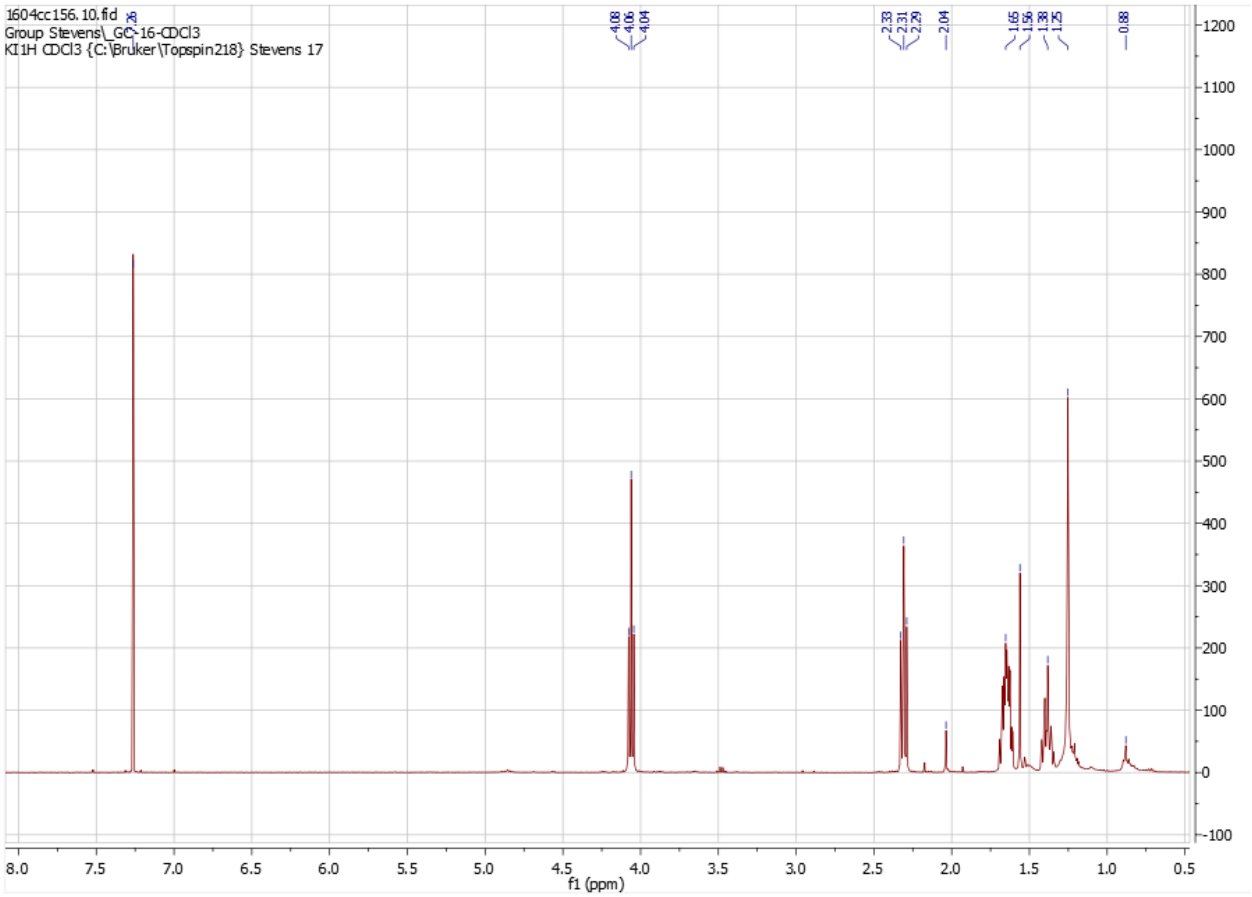

Figure 6.1.2 - [1] H-NMR spectrum of the HA – BP in chloroform.

6.2. Estimations on physiochemical properties for the HA-BP using Pepcalc.com

N-terminus	Sequence	C-terminus	AA code used	
▼	CGGGRYPISRPRKR	▼	single-lett ▼	Calculate!
	Disulphide connectivity			

Show abbreviations | 20 standard amino acids | modified amino acids | unusual amino acids

Sequence submission

Single letter code: CGGGRYPISRPRKR

Get a quotation

Sequence interpretation

Single letter code: NH2- CGGGRYPISR PRKR -COOH
Triple letter code: NH2- Cys - Gly - Gly - Gly - Arg - Tyr - Pro - Ile - Ser - Arg - Pro - Arg - Lys - Arg -COOH

Physiochemical properties

Number of residues:	14	
Molecular weight:	1602.87 g/mol	*notes on MW*
Extinction coefficient:	1280 $M^{-1}cm^{-1}$	*notes on Ext. Coefficient*
Iso-electric point:	pH 11.7	*notes on pI*
Net charge at pH 7:	4.9	*notes on net charge*
Estimated solubility:	Good water solubility.	*notes on solubility*

Net charge vs pH

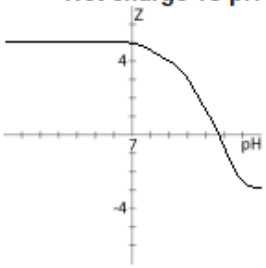

Hydropathy

Hopp & Woods

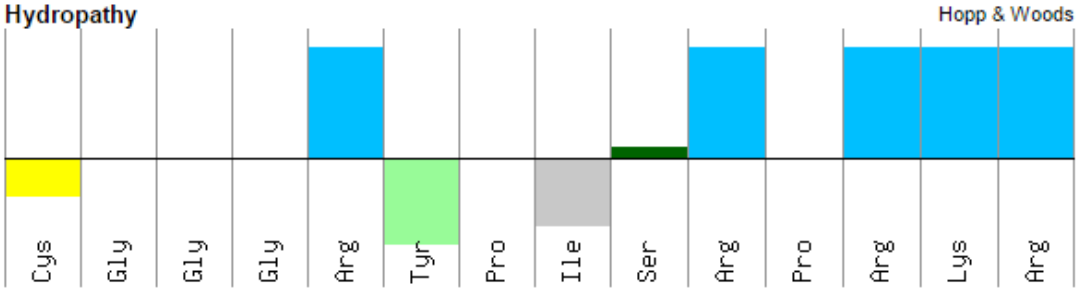

Top is hydrophilic
Bottom is hydrophobic
Color codes: Acidic | Aromatic | Basic | Aliphatic | Polar | Cysteine

6.3. Characterization of the biotinylated PEG monomer

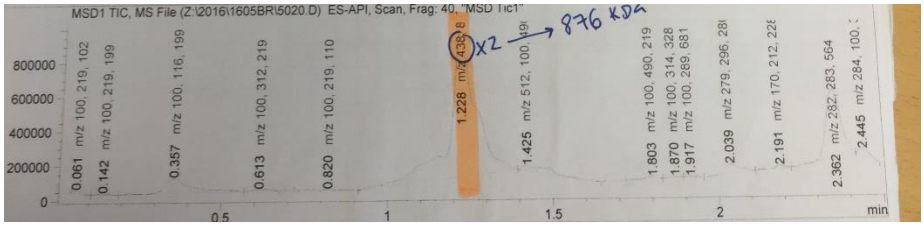

Figure 6.3.1 – ESI-MS mass spectrum of the biotinylated PEG monomer sample.

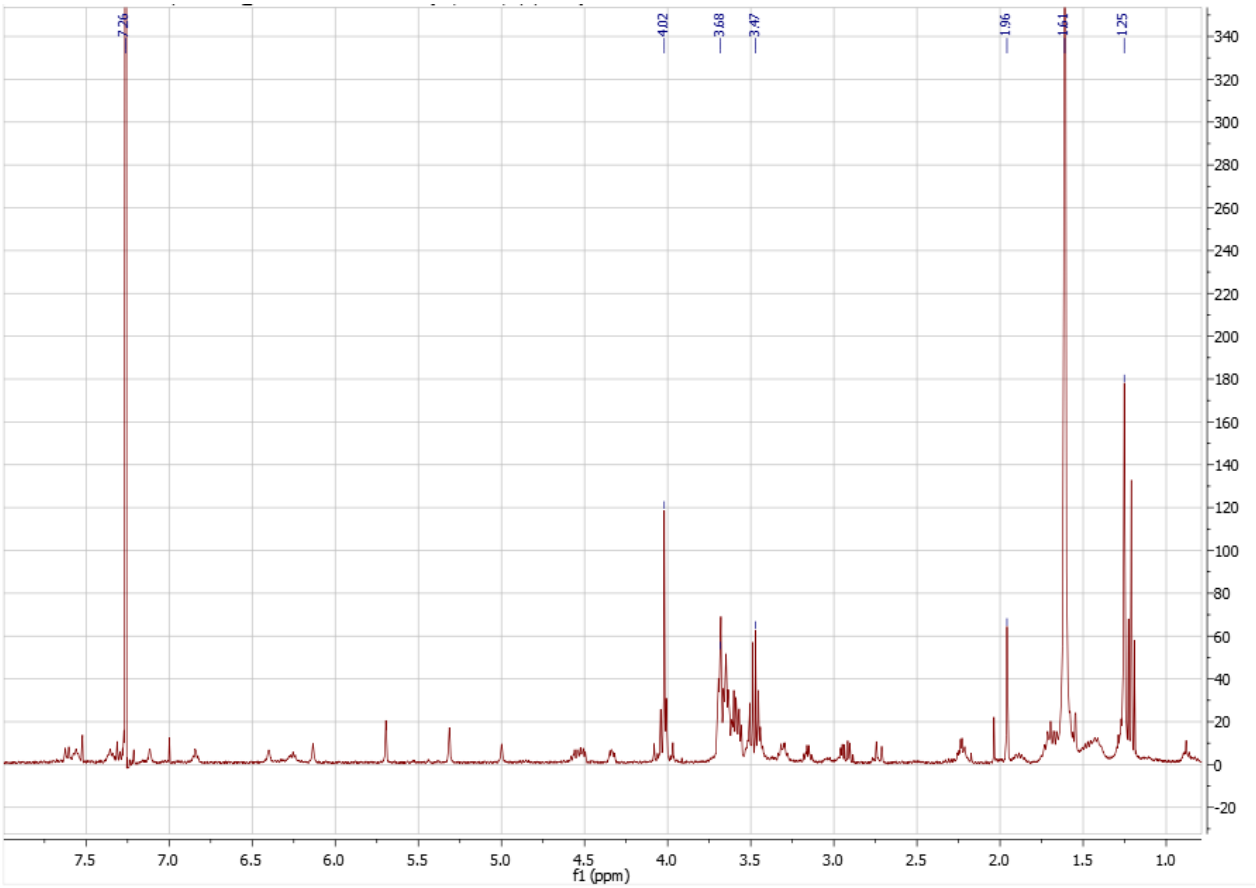

Figure 6.3.2 – [1] H-NMR spectrum of the biotinylated PEG monomer sample in chloroform. [1]H-NMR (400 MHz, CDCl3) δ ppm: 8.08 – 7.90 (s, 1H, NH), 7.75 – 7.60 (m, 3H, NH), 7.59 – 7.37 (s, 2H, NH), 7.21 – 6.93 (m, 3H, NH), 6.70 – 6.55 (m, 2H, NH), 6.44 – 6.33 (m, 2H, NH), 5.75 (s, 1H, H2C=C), 5.41 (s, 1H, H2C=C), 4.8 – 4.5 (m, 2H, biotin), 4.45 (m, 1H, α-Lys), 4.10 (s, 6H, -HNCO-CH2-O-), 3.91 – 3.44 (m, 26H, O-CH2- CH2-, -H2C-NHCO-), 3.43 – 3.29 (m, 1H, biotin), 3.28 – 3.17 (m, 2H, biotin), 2.43 – 2.27 (m, 2H, biotin), 1.99 (s, 3H, CH3-C=CH2), 1.95 – 1.36 (m, 12H, biotin and Lys CH2) (from Harrison et al. 2015[47])

6.4. SEC data from the ARGET ATRP polymerization assays

Vial A

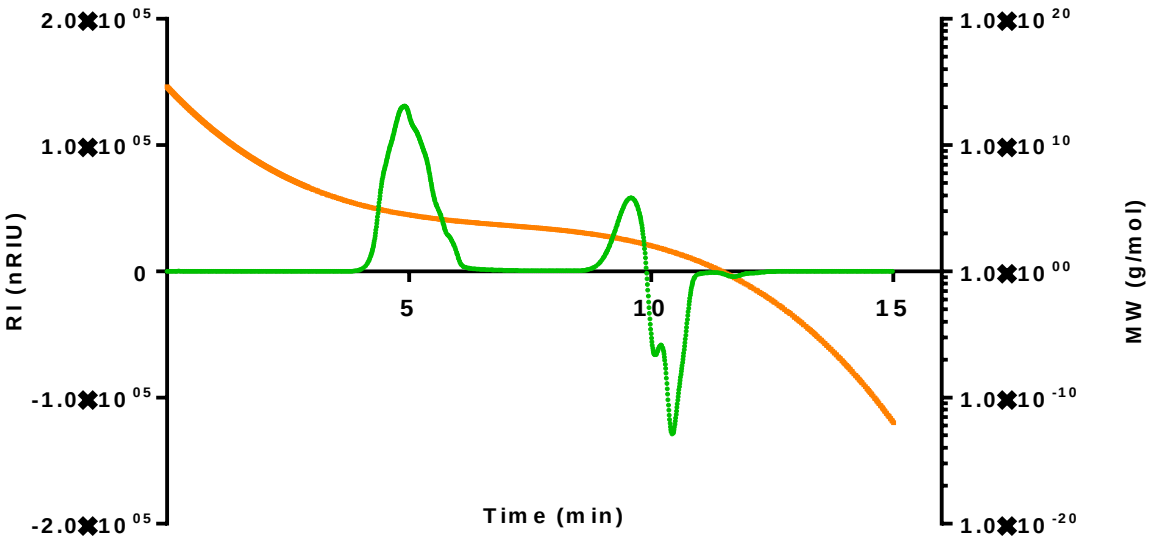

Vial B

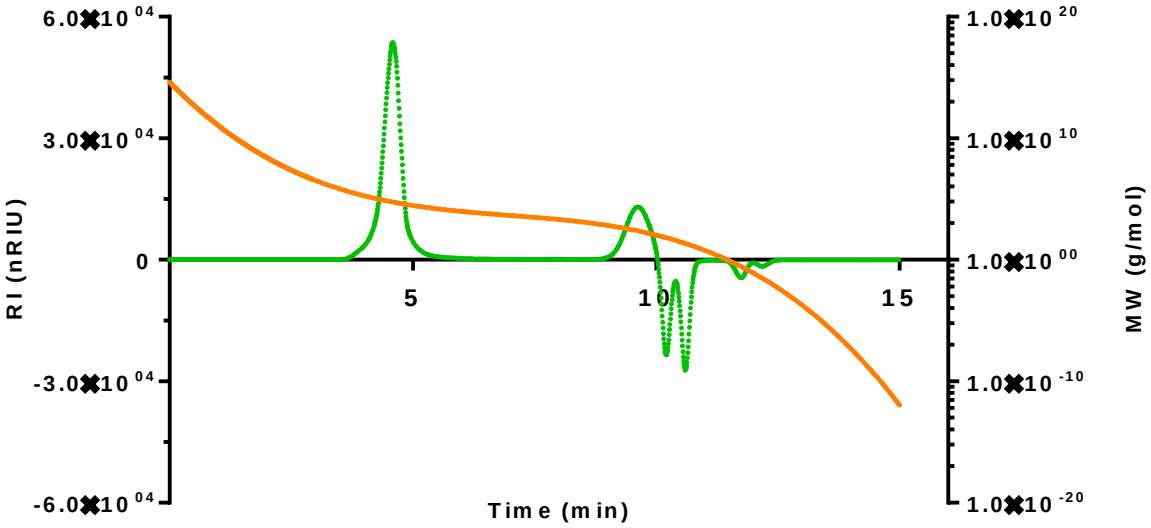

Vial C

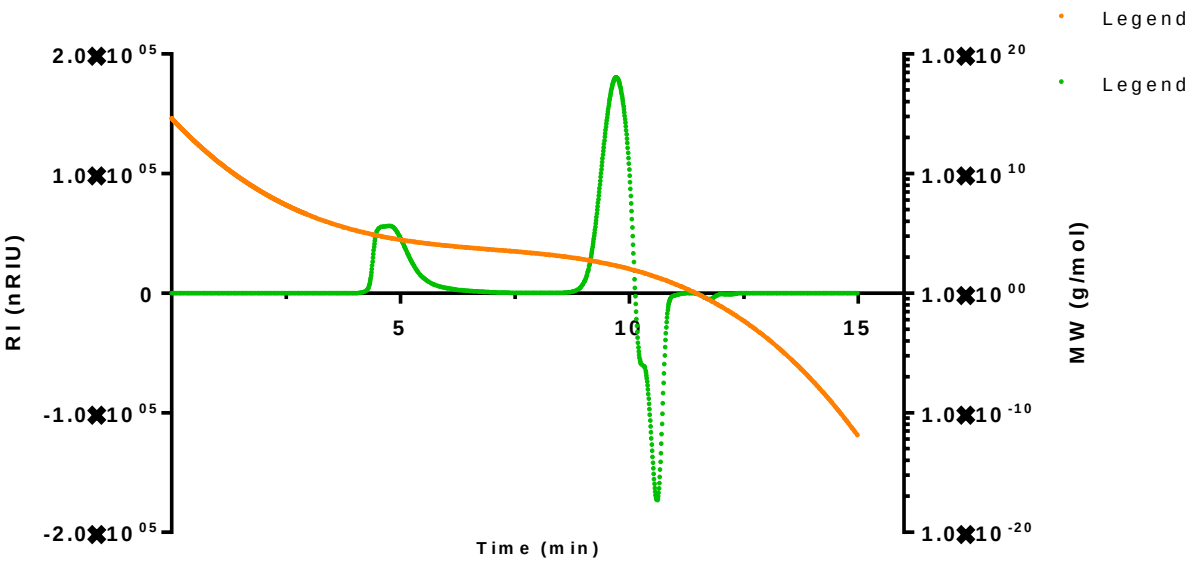
Legend
Legend
2.0✖10 05
1.0✖10 05
0
-1.0✖10 05
-2.0✖10 05
5
10
15
Time (min)
RI (nRIU)
1.0✖10 20
1.0✖10 10
1.0✖10 00
1.0✖10 -10
1.0✖10 -20
MW (g/mol)

Vial D

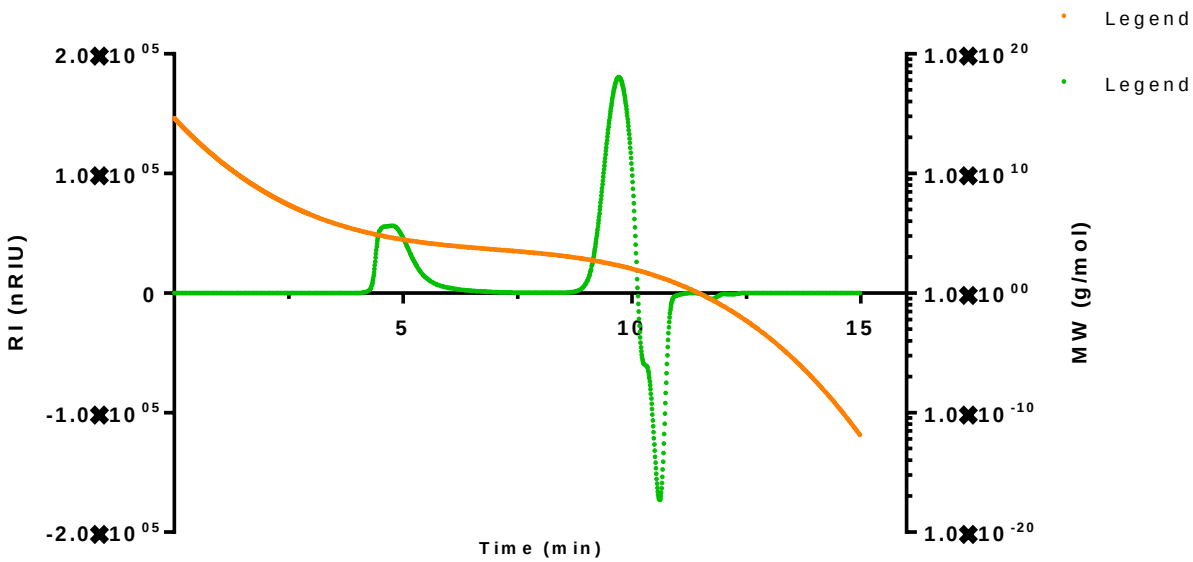
Legend
Legend
2.0✖10 05
1.0✖10 05
0
-1.0✖10 05
-2.0✖10 05
5
10
15
Time (min)
RI (nRIU)
1.0✖10 20
1.0✖10 10
1.0✖10 00
1.0✖10 -10
1.0✖10 -20
MW (g/mol)

Vial E

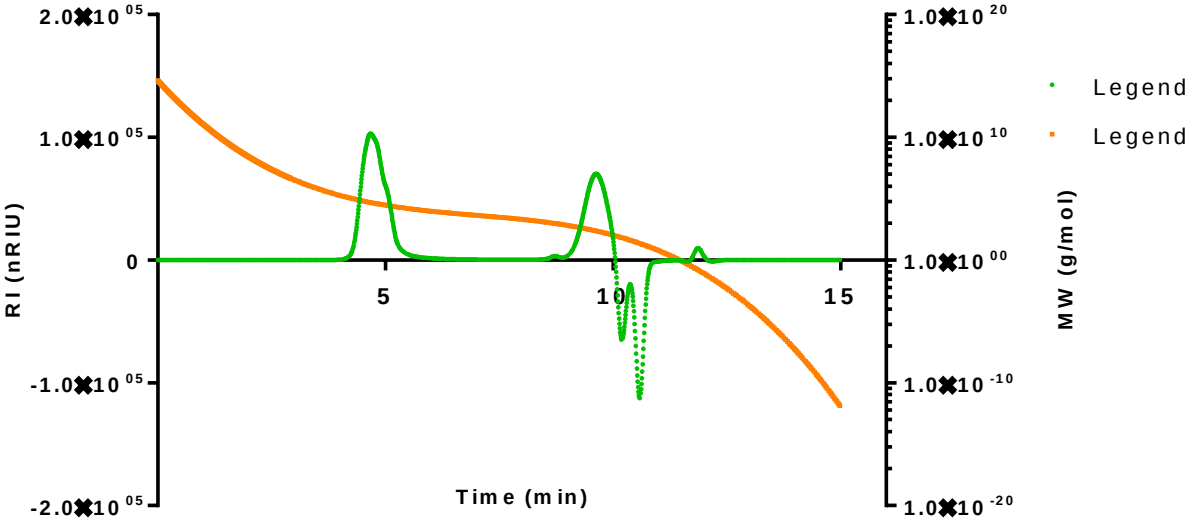
2.0✖10 05
1.0✖10 05
0
-1.0✖10 05
-2.0✖10 05
RI (nRIU)
5
10
15
Time (min)
1.0✖10 20
1.0✖10 10
1.0✖10 00
1.0✖10 -10
1.0✖10 -20
MW (g/mol)
Legend
Legend

6.5. G-code programs for melt electrospinning assays

6.5.1. Fiber diameter tests – 5 speeds, 0.5 mm spacing with stabilization of the fibers

```
G17 G21 G40 G49 G54 G80 G91 G94 F500

%% MAIN BODY OF CODE %%

G1 x25          % move 25mm from start point, towards center of plate

M98 p1233       % run program 1233

G1 x-65         % move 65mm back to original zero point

M30             % end program and rewind

%% PRIMARY PROGRAM %%

o1233           % Primary Program, 5 speed tests on 24x50mm coverslip, 5mm spacing, with stabilisation
M98 p1235       % Stabilisation run
M98 p1234 l4    % 8 passes on the slide
G1 x5           % move over 5 mm on the slide

F750            % increase speed to 750 mm/s
M98 p1235       % Stabilisation run
M98 p1234 l4    % 8 passes on the slide
G1 x5           % move over 5 mm on the slide

F1000           % increase speed to 1000 mm/s
M98 p1235       % Stabilisation run
M98 p1234 l4    % 8 passes on the slide
G1 x5           % move over 5 mm on the slide

F1250           % increase speed to 1250 mm/s
M98 p1235       % Stabilisation run
M98 p1234 l4    % 8 passes on the slide
G1 x5           % move over 5 mm on the slide

F1500           % increase speed to 1500 mm/s
M98 p1235       % Stabilisation run
M98 p1234 l4    % 8 passes on the slide

M99             % End Primary Program 1233

%% SECONDARY PROGRAMS %%

o1235           % Secondary Program 1235 - Stabilisation Run
G1 y60          % move down the plate 60 mm
M98 p1234 l40   % 80 passes to stabilise
G1 x-40         % back to original x coordinate
G1 y-60         % back to top of slide
M99             % End secondary program 1235

o1234           % Secondary Program 1234 - Printing on Slide
G1 x0 y0% define start point
G1 y+24.000000  % Print down across slide
G1 x0.5         % move over 500 um
G1 y-24.000000  % Print up across slide
G1 x0.5         % move over 500 um
M99             % End secondary program 1234

M2              % End Program
```

6.5.2.3x3 cm scaffolds, 0.5 mm pores

```
G17 G21 G40 G49 G54 G80 G91 G94 F1000   %G91 is relative coordinates!

G1 x20.000000

M98 p1233 l30

M30

o1233
M98 p1234 l30    % loop size/FD
G1 x30.000000
G1 y-30.000000
M98 p1235 l30    %loop size/FD
M99

o1234
G1 x0 y0
G1 x30.000000
G1 y0.5
G1 x-30.00000
G1 y0.5
M99

o1235
G1 x-0.5
G1 y30.00000
G1 x-0.5
G1 y-30.00000
M99

M2
```

6.6. SEC analysis for the 50% (w/w) 45-80 kDa PCL before and after printing assays (3 to 4 weeks)

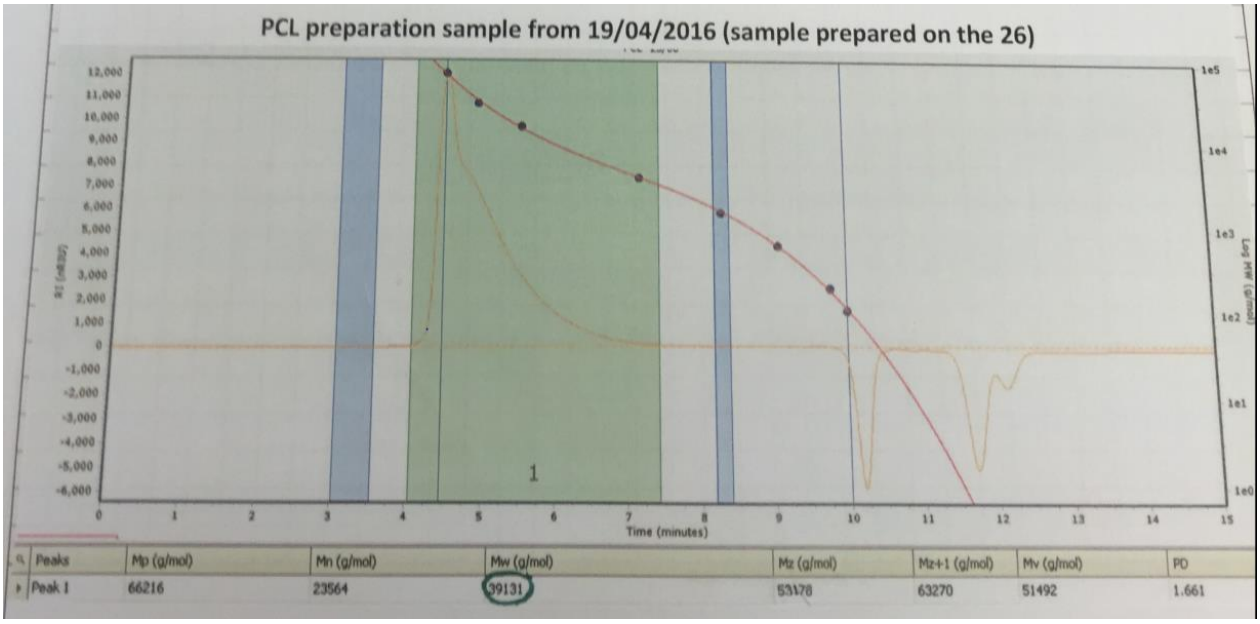

Figure 6.6.1 – SEC analysis for the sample of the blend before starting the printing assays.

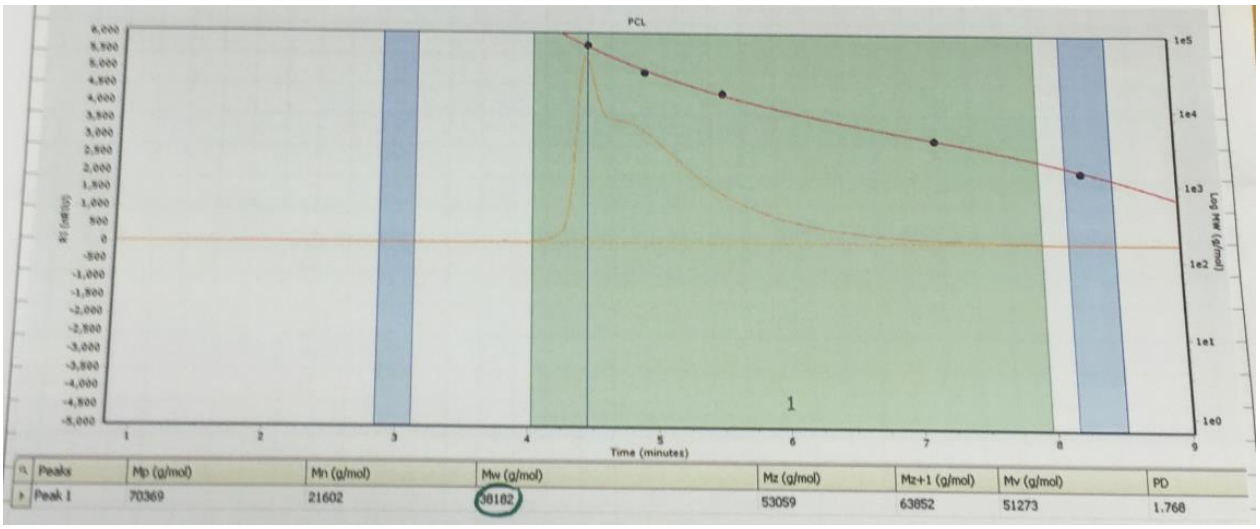

Figure 6.6.2 – SEC analysis for the sample of the blend after three to four weeks of printing assays.

7. References

1. Seo, S.-J., Mahapatra, C., Singh, R. K., Knowles, J. C. & Kim, H.-W. Strategies for osteochondral repair: Focus on scaffolds. *J. Tissue Eng.* **5,** 2041731414541850 (2014).

2. Li, X., Ding, J., Wang, J., Zhuang, X. & Chen, X. Biomimetic biphasic scaffolds for osteochondral defect repair. *Regen. Biomater.* **2,** 221–228 (2015).

3. McMahon, L., O'Brien, F. & Prendergast, P. Biomechanics and mechanobiology in osteochondral tissues. *Regen. Med.* **3,** 743–759 (2008).

4. Stevens, M. M. Biomaterials for bone tissue engineering. *Mater. Today* **11,** 18–25 (2008).

5. http://therapydiaportland.com/happy-joints/.

6. JONES, A. *et al.* Assessment of bone ingrowth into porous biomaterials using MICRO-CT. *Biomaterials* **28,** 2491–2504 (2007).

7. Müller, B. *et al.* Bio-mimetic hollow scaffolds for long bone replacement. *Proc. SPIE* **7401,** 74010D–74010D–13 (2009).

8. HABIBOVIC, P. *et al.* Osteoconduction and osteoinduction of low-temperature 3D printed bioceramic implants. *Biomaterials* **29,** 944–953 (2008).

9. Murphy, C. M., Haugh, M. G. & O'Brien, F. J. The effect of mean pore size on cell attachment, proliferation and migration in collagen–glycosaminoglycan scaffolds for bone tissue engineering. *Biomaterials* **31,** 461–466 (2010).

10. Woodard, J. R. *et al.* The mechanical properties and osteoconductivity of hydroxyapatite bone scaffolds with multi-scale porosity. *Biomaterials* **28,** 45–54 (2007).

11. Whang, K. *et al.* Engineering Bone Regeneration with Bioabsorbable Scaffolds with Novel Microarchitecture. *Tissue Eng.* **5,** 35–51 (1999).

12. Ristovski, N. *et al.* Improved fabrication of melt electrospun tissue engineering scaffolds using direct writing and advanced electric field control. *Biointerphases* **10,** 11006 (2015).

13. Khaled, E. G., Saleh, M., Hindocha, S., Griffin, M. & Khan, W. S. Tissue Engineering for Bone Production-Stem Cells, Gene Therapy and Scaffolds. *Open Orthop. J.* **5,** 289–295 (2011).

14. Albrektsson, T. & Johansson, C. Osteoinduction, osteoconduction and osseointegration. *Eur. Spine J.* **10,** 96–101 (2001).

15. Das, K., Balla, V. K., Bandyopadhyay, A. & Bose, S. Surface modification of laser-processed porous titanium for load-bearing implants. *Scr. Mater.* **59,** 822–825 (2008).

16. Ren, J. *et al.* Melt-electrospun polycaprolactone-strontium substituted bioactive glass scaffolds for bone regeneration. *J. Biomed. Mater. Res. A* **61,** 1–41 (2013).

17. Bose, S. & Roy, M. Recent Advances in Bone Tissue Engineering Scaffolds. *Trends Biotechnol* **30,** 546–554 (2013).

18. Lichte, P., Pape, H. C., Pufe, T., Kobbe, P. & Fischer, H. Scaffolds for bone healing: Concepts, materials and evidence. *Injury* **42,** 569–573 (2011).

19. Wu, G.-H. & Hsu, S. Review: Polymeric-Based 3D Printing for Tissue Engineering. *J. Med. Biol. Eng.* **35,** 285–292 (2015).

20. Olivares, A. L., Marsal, È., Planell, J. a. & Lacroix, D. Finite element study of scaffold architecture design and culture conditions for tissue engineering. *Biomaterials* **30,** 6142–6149 (2009).

21. Callister, W. D. *Materials Science and Engineering*. (Wiley & Sons, 2007).

22. Kucharska, M., Butruk, B., Walenko, K., Brynk, T. & Ciach, T. Fabrication of in-situ foamed chitosan/β-TCP scaffolds for bone tissue engineering application. *Mater. Lett.* **85,** 124–127 (2012).

23. Szkodo, M. Clay Minerals – Mineralogy and Phenomenon of Clay Swelling in Oil & Gas Industry. 3–9 (2015). doi:10.1515/adms

24. Zhu, N. & Chen, X. in *Advances in Biomaterials Science and Biomedical Applications* 315–328 (INTECH, 2013). doi:10.5772/56420

25. Sultana, N. & Wang, M. Fabrication of HA/PHBV composite scaffolds through the emulsion freezing/freeze-drying process and characterisation of the scaffolds. *J. Mater. Sci. Mater. Med.* **19,** 2555–2561 (2008).

26. Seol, Y.-J. *et al.* Chitosan sponges as tissue engineering scaffolds for bone formation. *Biotechnol. Lett.* **26,** 1037–1041 (2004).

27. Hutmacher, D. W. Scaffolds in tissue engineering bone and cartilage. *Biomaterials* **21,** 2529–2543 (2000).

28. Nam, Y. S. & Park, T. G. Porous biodegradable polymeric scaffolds prepared by thermally induced phase separation. *J. Biomed. Mater. Res.* **47,** 8–17 (1999).

29. Akbarzadeh, R. & Yousefi, A.-M. Effects of processing parameters in thermally induced phase separation technique on porous architecture of scaffolds for bone tissue engineering. *J. Biomed. Mater. Res. Part B Appl. Biomater.* **102,** 1304–1315 (2014).

30. Mikos, A. G., Sarakinos, G., Leite, S. M., Vacanti, J. P. & Langer, R. Laminated three-dimensional biodegradable foams for use in tissue engineering. *Biomater. Silver Jubil. Compend.* **14,** 93–100 (2006).

31. Yoshikawa, H., Tamai, N., Murase, T. & Myoui, A. Interconnected porous hydroxyapatite ceramics for bone tissue engineering. *J. R. Soc. Interface* **6 Suppl 3,** S341–S348 (2009).

32. Bose, S., Vahabzadeh, S. & Bandyopadhyay, A. Bone tissue engineering using 3D printing. *Mater. Today* **16,** 496–504 (2013).

33. Chen, Q.; Roether, J.A.; Boccaccini, A. R. in *Topics in Tissue Engineering* **4,** 1–27 (2008).

34. Siva, A. P. S. & Ansari, M. N. M. A Review on Bone Scaffold Fabrication Methods. 1232–1238 (2015).

35. Chen, G., Ushida, T. & Tateishi, T. Scaffold design for tissue engineering. *Macromol. Biosci.* **2,** 67–77 (2002).

36. Katz, J. L., Ambrose, C. G., Mcmillin, C. & Spencer, P. Encyclopedia of biomaterials and biomedical engineering. *Orthopedic biomaterials* (2004).

37. Dalton, P. D. *et al.* Electrospinning and additive manufacturing: converging technologies. *Biomater.*

Sci. **1,** 171–185 (2013).

38. Chia, H. N. & Wu, B. M. Recent advances in 3D printing of biomaterials. *J. Biol. Eng.* **9,** 4 (2015).

39. Woodruff, M. A. & Hutmacher, D. W. The return of a forgotten polymer—Polycaprolactone in the 21st century. *Prog. Polym. Sci.* **35,** 1217–1256 (2010).

40. Hochleitner, G. *et al.* Additive manufacturing of scaffolds with sub-micron filaments via melt electrospinning writing. *Biofabrication* **7,** 35002 (2015).

41. Brown, T. D., Dalton, P. D. & Hutmacher, D. W. Direct Writing By Way of Melt Electrospinning. *Adv. Mater.* **23,** 5651–5657 (2011).

42. Ducheyne, P. *Comprehensive Biomaterials*. (Elsevier Science, 2011).

43. Uquillas Paredes, J. A., Polini, A. & Chrzanowski, W. Protein-based Biointerfaces to Control Stem Cell Differentiation. 1–29 doi:10.1039/9781782628453-00001

44. Mager, M. D., LaPointe, V. & Stevens, M. M. Exploring and exploiting chemistry at the cell surface. *Nat. Chem.* **3,** 582–589 (2011).

45. Germanier, Y., Tosatti, S., Broggini, N., Textor, M. & Buser, D. Enhanced bone apposition around biofunctionalized sandblasted and acid-etched titanium implant surfaces: A histomorphometric study in miniature pigs. *Clin. Oral Implants Res.* **17,** 251–257 (2006).

46. Kroese-Deutman, H. C., van den Dolder, J., Spauwen, P. H. M. & Jansen, J. a. Influence of RGD-loaded titanium implants on bone formation in vivo. *Tissue Eng.* **11,** 1867–1875 (2015).

47. Harrison, R. H. *et al.* Modular and Versatile Spatial Functionalization of Tissue Engineering Scaffolds through Fiber-Initiated Controlled Radical Polymerization. *Adv. Funct. Mater.* **25,** 5748–5757 (2015).

48. Chow, L. W. *et al.* Peptide-directed spatial organization of biomolecules in dynamic gradient scaffolds. *Adv. Healthc. Mater.* **3,** 1381–1386 (2014).

49. Pierschbacher, M. D. & Ruoslahti, E. Cell attachment activity of fibronectin can be duplicated by small synthetic fragments of the molecule. *Nature* **309,** 30–33 (1984).

50. Petrie, T. A., Capadona, J. R., Reyes, C. D. & García, A. J. Integrin specificity and enhanced cellular activities associated with surfaces presenting a recombinant fibronectin fragment compared to RGD supports. *Biomaterials* **27,** 5459–5470 (2006).

51. Ruoslahti, E. & Pierschbacher, M. D. New perspectives in cell adhesion: RGD and integrins. *Science* **238,** 491–7 (1987).

52. Delforge, D., Gillon, B., Art, M. & Dewelle, J. Design of a synthetic adhesion protein by grafting RGD tailed cyclic peptides on bovine serum albumin. *… J. Pept. …* 87–91 (1998). doi:10.1023/A:1008880124720

53. Bone, A. *et al.* Bone Sialoprotein Peptides Are Potent Inhibitors of Breast Cancer Cell. 1948–1955 (1955).

54. Matsumura, S. *et al.* Ionomers for proton exchange membrane fuel cells with sulfonic acid groups on the end-groups: Novel branched poly(ether-ketone)s. *Am. Chem. Soc. Polym. Prepr. Div. Polym. Chem.* **49,** 511–512 (2008).

55. Harrison, R. H. Engineered Scaffolds for the Preservation of Gliding Tissue Interfaces. (Imperial College London, UK, 2016).

56. Chandrudu, S., Simerska, P. & Toth, I. Chemical methods for peptide and protein production. *Molecules* **18,** 4373–4388 (2013).

57. Carpino, L. A. & Han, G. Y. 9-Fluorenylmethoxycarbonyl function, a new base-sensitive amino-protecting group. *J. Am. Chem. Soc.* **92,** 5748–5749 (1970).

58. Behrendt, R., White, P. & Offer, J. Advances in Fmoc solid-phase peptide synthesis. *J. Pept. Sci.* **22,** 4–27 (2016).

59. Duro-Castano, A., Conejos-Sánchez, I. & Vicent, M. J. Peptide-based polymer therapeutics. *Polymers (Basel).* **6,** 515–551 (2014).

60. Coessens, V., Pintauer, T. & Matyjaszewski, K. Functional polymers by atom transfer radical polymerization. *Prog. Polym. Sci.* **26,** 337–377 (2001).

61. Billmeyer, F. W. *Textbook of Polymer science*. (John Wiley & Sons, Inc., 1971).

62. Oh, J. K., Min, K. & Matyjaszewski, K. Preparation of poly(oligo(ethylene glycol) monomethyl ether methacrylate) by homogeneous aqueous AGET ATRP. *Macromolecules* **39,** 3161–3167 (2006).

63. Matyjaszewski, K. Atom Transfer Radical Polymerization (ATRP): Current status and future perspectives. *Macromolecules* **45,** 4015–4039 (2012).

64. Telford, A. M. *et al.* Micropatterning of polymer brushes: Grafting from dewetting polymer films for biological applications. *Biomacromolecules* **13,** 2989–2996 (2012).

65. Lavanant, L. *et al.* Polymer Brushes via Surface-Initiated Controlled Radical Polymerization : Synthesis , Characterization , Properties , and Applications. 5437–5527 (2009).

66. Yano, T. *et al.* Precise control of surface physicochemical properties for electrospun fiber mats by surface-initiated radical polymerization. *Polym. J.* **43,** 838–848 (2011).

67. Banerjee, S., Paira, T. K. & Mandal, T. K. Surface confined atom transfer radical polymerization: access to custom library of polymer-based hybrid materials for speciality applications. *Polym. Chem.* **5,** 4153–4167 (2014).

68. Yoshikawa, C., Zhang, K., Zawadzak, E. & Kobayashi, H. A novel shortened electrospun nanofiber modified with a 'concentrated' polymer brush. *Sci. Technol. Adv. Mater.* **12,** 15003 (2011).

69. Tugulu, S. & Klok, H. A. Stability and nonfouling properties of poly(poly(ethylene glycol) methacrylate) Brushes under cell culture conditions. *Biomacromolecules* **9,** 906–912 (2008).

70. Knop, K., Hoogenboom, R., Fischer, D. & Schubert, U. S. Poly(ethylene glycol) in drug delivery: Pros and cons as well as potential alternatives. *Angew. Chemie - Int. Ed.* **49,** 6288–6308 (2010).

71. Banerjee, I., Pangule, R. C. & Kane, R. S. Antifouling coatings: Recent developments in the design of surfaces that prevent fouling by proteins, bacteria, and marine organisms. *Adv. Mater.* **23,** 690–718 (2011).

72. Zalipsky, S. Functionalized poly(ethylene glycol) for preparation of biologically relevant conjugates. *Bioconjug. Chem.* **6,** 150–165 (1995).

73. Muerza-Cascante, M. L., Haylock, D., Hutmacher, D. W. & Dalton, P. D. Melt Electrospinning and Its Technologization in Tissue Engineering. *Tissue Eng. Part B. Rev.* **0,** 1–16 (2014).

74. Dalton, P. D. *et al.* Electrospinning and additive manufacturing: converging technologies. *Biomater. Sci.* **1,** 1–27 (2013).

75. Mammadov, B., Sever, M., Guler, M. O. & Tekinay, A. B. Neural differentiation on synthetic scaffold materials. *J. Biomater. Sci. Polym. Ed.* **1,** 1119–1137 (2013).

76. Liu, T., Houle, J. D., Xu, J., Chan, B. P. & Chew, S. Y. Nanofibrous collagen nerve conduits for spinal cord repair. *Tissue Eng. Part A* **18,** 1057–66 (2012).

77. Lyons, J., Li, C. & Ko, F. Melt-electrospinning part I: Processing parameters and geometric properties. *Polymer (Guildf).* **45,** 7597–7603 (2004).

78. Brown, T. D., Dalton, P. D. & Hutmacher, D. W. Melt electrospinning today: An opportune time for an emerging polymer process. *Prog. Polym. Sci.* (2015). doi:10.1016/j.progpolymsci.2016.01.001

79. Nayak, R., Kyratzis, I. L., Truong, Y. B., Padhye, R. & Arnold, L. Melt-electrospinning of polypropylene with conductive additives. *J. Mater. Sci.* **47,** 6387–6396 (2012).

80. Blount, M. J. & Lister, J. R. The asymptotic structure of a slender dragged viscous thread. *J. Fluid Mech.* **674,** 489–521 (2011).

81. Kim, S. J., Jang, D. H., Park, W. H. & Min, B. M. Fabrication and characterization of 3-dimensional PLGA nanofiber/microfiber composite scaffolds. *Polymer (Guildf).* **51,** 1320–1327 (2010).

82. Charuchinda, A., Molloy, R., Siripitayananon, J., Molloy, N. & Sriyai, M. Factors influencing the small-scale melt spinning of poly(??-caprolactone) monofilament fibres. *Polym. Int.* **52,** 1175–1181 (2003).

83. Natta, F., Hill, J. & Carothers, W. Studies of Polymerization and Ring Formation. XXIII. 1 Îµ-Caprolactone and its Polymers. *J. Am. Chem. Soc.* **1772,** 5–7 (1934).

84. Woodward, S. C., Brewer, P. S., Moatamed, F., Schindler, A. & Pitt, C. G. The intracellular degradation of poly(??-caprolactone). *J. Biomed. Mater. Res.* **19,** 437–444 (1985).

85. Lam, C. X. F., Hutmacher, D. W., Schantz, J.-T., Woodruff, M. A. & Teoh, S. H. Evaluation of polycaprolactone scaffold degradation for 6 months in vitro and in vivo. *J. Biomed. Mater. Res. A* **90,** 906–919 (2009).

86. Qin, Y. Alginate fibers: an overwiew of the production processes and applications in wound management. *Polym. Int.* **57,** 171–180 (2008).

87. Grafts, C. T. B., Part, I. & Eng, T. Repair of Calvarial Defects with. **9,** (2003).

88. Sawyer, A. A. *et al.* The stimulation of healing within a rat calvarial defect by mPCL-TCP/collagen scaffolds loaded with rhBMP-2. *Biomaterials* **30,** 2479–2488 (2009).

89. Fu, G. D. *et al.* Core - Sheath nanofibers from combined atom transfer radical polymerization and electrospinning. *Macromolecules* **41,** 6854–6858 (2008).

90. Zhang, Q., Lu, H., Kawazoe, N. & Chen, G. Pore size effect of collagen scaffolds on cartilage regeneration. *Acta Biomater.* **10,** 2005–2013 (2014).

91. Gentsch, R. *et al.* Single-step electrospinning to bioactive polymer nanofibers. *Macromolecules* **44,** 453–461 (2011).

92. Fox, T. G. & Loshaek, S. Isothermal Viscosity-Molecular Weight Dependence for Long Polymer Chains. *J. Appl. Phys.* **26,** 1080 (1955).

93. Fox, T. G. & Loshaek, S. Influence of molecular weight and degree of crosslinking on the specific volume and glass temperature of polymers. *J. Polym. Sci.* **15,** 371–390 (1955).